

Parvalbumin and somatostatin interneurons contribute to the generation of hippocampal gamma oscillations

Pantelis Antonoudiou¹, Yu Lin Tan¹, Georgina Kontou³, A. Louise Upton^{1,2} and Edward O. Mann^{1,2}

¹Department of Physiology, Anatomy and Genetics, University of Oxford, Oxford, OX1 3PT, UK

²Oxford Ion Channel Initiative, University of Oxford, OX1 3PT, Oxford, UK

³Neuroscience, Physiology and Pharmacology, University College London

Corresponding author's electronic address: ed.mann@dpag.ox.ac.uk

Abbreviated title: Role of PV+ and SST+ interneurons in γ oscillations.

Both male and female sexes were studied.

Number of Pages: 53

Number of Figures: 9

Number of Tables: 1

Number of words: Abstract = 156, Introduction = 650, Discussion = 1500.

The authors declare no conflicting financial interests.

Acknowledgments: We would like to thank the MRC for funding provision. We would also like to thank Dr. Alexandru Calin for providing the SST mouse colony.

25 **Abstract**

26 Gamma-frequency oscillations (30-120 Hz) in cortical networks influence neuronal encoding and
27 information transfer, and are disrupted in multiple brain disorders. While synaptic inhibition is
28 important for synchronization across the gamma-frequency range, the role of distinct interneuronal
29 subtypes in slow (< 60 Hz) and fast gamma states remains unclear. Here, we used optogenetics to
30 examine the involvement of parvalbumin (PV+) and somatostatin (SST+) expressing interneurons in
31 gamma oscillations in the mouse hippocampal CA3 *ex vivo*, using animals of either sex. Disrupting
32 either PV+ or SST+ interneuron activity, via either photo-inhibition or photo-excitation, led to a
33 decrease in the power of cholinergically-induced slow gamma oscillations. Furthermore, photo-
34 excitation of SST+ interneurons induced fast gamma oscillations, which depended on both synaptic
35 excitation and inhibition. Our findings support a critical role for both PV+ and SST+ interneurons in
36 slow hippocampal gamma oscillations, and further suggest that intense activation of SST+
37 interneurons can enable the CA3 circuit to generate fast gamma oscillations.

38

39 **Significance statement:** The generation of hippocampal gamma oscillations depends on
40 synchronised inhibition provided by GABAergic interneurons. Parvalbumin expressing (PV+)
41 interneurons are thought to play the key role in coordinating the spike timing of excitatory
42 pyramidal neurons, but the role distinct inhibitory circuits in network synchronisation remains
43 unresolved. Here, we show for the first time that causal disruption of either PV+ or somatostatin
44 expressing (SST+) interneuron activity impairs the generation of slow gamma oscillations in the
45 ventral hippocampus *ex vivo*. We further show that SST+ interneuron activation along with general
46 network excitation is sufficient to generate high frequency gamma-oscillations in the same
47 preparation. These results affirm a crucial role for both PV+ and SST+ interneurons in hippocampal
48 gamma oscillation generation.

49

50 **Introduction**

51 Gamma oscillations (30 - 120 Hz) are a common feature of active cortical networks, which have been
52 proposed to contribute to local gain control (Sohal *et al.*, 2009; Cardin *et al.*, 2009; Sohal, 2016) and
53 facilitate transmission between synchronised neuronal assemblies (Fries, 2005; Akam & Kullmann,

2010; Fries, 2015). While the function of gamma oscillations remains debated (Burns, Xing & Shapley, 2011; Butler & Paulsen, 2014; Bastos, Vezoli & Fries, 2015; Ray & Maunsell, 2015; Womelsdorf & Everling, 2015; Lasztóczy & Klausberger, 2016; Sohal, 2016), changes in these rhythms continue to act as a useful marker of function and dysfunction in cortical circuit operations (Bragin *et al.*, 1995; Fries *et al.*, 2001; Herrmann & Demiralp, 2005; Uhlhaas & Singer, 2006; Basar-Eroglu *et al.*, 2007; Uhlhaas & Singer, 2010; Yamamoto *et al.*, 2014; Spellman *et al.*, 2015). There is a general consensus that the generation of gamma rhythms depends upon the spiking of inhibitory interneurons, which synchronise the firing of excitatory pyramidal cells via fast synaptic inhibition (Whittington, Traub & Jefferys, 1995; Penttonen *et al.*, 1998; Csicsvari *et al.*, 2003; Hájos *et al.*, 2004; Mann *et al.*, 2005; Hasenstaub *et al.*, 2005; Bartos, Vida & Jonas, 2007; Buzsáki & Wang, 2012; Kim *et al.*, 2016; Chen *et al.*, 2017; Veit *et al.*, 2017). Specifically, parvalbumin-expressing (PV+) interneurons, which target the perisomatic domain of pyramidal neurons, are thought to play the key role in generating and maintaining gamma oscillations in the brain (Csicsvari *et al.*, 2003; Hájos *et al.*, 2004; Mann *et al.*, 2005; Gloveli *et al.*, 2005; Hájos & Paulsen, 2009; Tukker *et al.*, 2013; Cardin, 2016; Penttonen *et al.*, 1998). PV+ interneurons are adapted for fast synchronisation of network activity, as they resonate at gamma frequencies and exert strong perisomatic inhibition that is capable of precisely controlling spike timing (Pike *et al.*, 2000; Pouille & Scanziani, 2001; Cardin *et al.*, 2009; Bartos & Elgueta, 2012; Hu, Gan & Jonas, 2014; Kohus *et al.*, 2016).

Recently, a selective role for PV+ interneurons in gamma-frequency synchronisation has been challenged by several studies performed in the primary visual cortex (Chen *et al.*, 2017; Veit *et al.*, 2017; Hakim, Shamardani & Adesnik, 2018). In this brain region, it was shown that dendrite-targeting somatostatin-expressing (SST+) interneurons were the main contributors for the generation of slow gamma oscillations, while PV+ interneurons were more important for higher frequency synchronisation (Chen *et al.*, 2017). Previous studies have found analogous roles for SST+ and PV+ interneurons in low- and high-frequency network synchronisation (Beierlein, Gibson &

79 Connors, 2000; Gloveli *et al.*, 2005; Tukker *et al.*, 2007; Craig & McBain, 2015). However, it is not yet
80 clear whether SST+ interneurons might play a more generic role in the generation of slow gamma
81 oscillations across brain areas.

82 The hippocampus displays both slow and fast gamma rhythms during theta activity, with slow
83 gamma generated in CA3 and fast gamma propagated from entorhinal cortex (Bragin *et al.*, 1995;
84 Colgin *et al.*, 2009; Schomburg *et al.*, 2014; Lasztóczy & Klausberger, 2016). The circuitry for slow
85 gamma oscillations is preserved in hippocampal slices (Fisahn *et al.*, 1998), and these models have
86 been used extensively to show that PV+ interneurons are strongly phase-coupled to gamma
87 oscillations, and contribute to rhythmogenesis (Hájos *et al.*, 2004; Mann *et al.*, 2005; Gloveli *et al.*,
88 2005; Gulyás *et al.*, 2010). However, the majority of interneurons are phase-coupled to ongoing
89 slow gamma oscillations (Hájos *et al.*, 2004; Gloveli *et al.*, 2005; Oren *et al.*, 2006), and it may be
90 that SST+ interneurons play an important role in synchronising PV+ networks. Indeed, whether
91 specific classes of CA3 interneuron are necessary and sufficient for the generation of slow gamma
92 oscillations has not yet been tested. Here, we took advantage of optogenetic techniques (Nagel *et al.*,
93 2003; Chow *et al.*, 2010; Boyden *et al.*, 2005) to test the involvement of PV+ and SST+
94 interneurons in cholinergically-induced gamma oscillations in the CA3 of acute hippocampal slices.

95

96 **Materials and Methods**

97 **Transgenic mice**

98 All procedures were performed according to the United Kingdom Animals Scientific Procedures Act
99 (ASPA) 1986 and the University of Oxford guidelines. Adult (older than 8 weeks, both male and
100 female) PV-cre (B6;129P2-Pvalbtm1(cre)Arbr/J), PV-cre-Ai9 (PV-Cre x Gt ROSA (CAG-tdTomato)
101 Hze/J), and SST-cre mice (Sst tm2.1(cre)Zjh/J) were used for all experiments.

102

103 **Stereotaxic viral injections**

104 Anaesthesia was induced in mice with 4 % isoflurane/medical oxygen mixture (2 L per min). The area
105 around the head was shaved and cleaned in preparation for scalp incision. Anaesthesia was
106 subsequently maintained using 1.5 - 2.5 % isoflurane at a rate of 2 L per min. Before the onset of
107 the procedure a cocktail of systemic peri-operative analgesics (Metacam (Meloxicam) 1 mg/Kg and
108 Vetergesic (Buprenorphine) 0.1 mg/Kg) and a local analgesic (Marcaine (Bupivacaine) 10mg/Kg)
109 were administered subcutaneously (Oxford University Veterinary Services). Following, antibiotic
110 solution was applied on the head and an incision of the scalp was performed that allowed a small
111 craniotomy to be made. A 33/34-gauge needle was attached on a Hamilton Microliter Syringe and
112 used to inject the virus solution at a rate of ≈ 100 nL/min (viral concentration $\approx 10^{12}$ genome copies
113 per mL). After every injection, the needle was left stationary for at least three minutes to allow
114 diffusion of virus in the surrounding area. The virus solution was injected with the aid of a stereotaxic
115 frame into ventral CA3 area of hippocampus (2.7 mm caudal and 2.75 mm lateral from Bregma). A
116 total of 600 - 800 nL were injected at two depths (300 - 400 nL at 3.1 mm and 300 - 400 nL at 2.7
117 mm). Following the injection, local analgesic (Marcaine 10 mg/Kg) was applied on the incised scalp
118 before it was sutured. The animals were then transferred in a heating chamber and allowed to
119 recover. The animals were monitored, and welfare scored in the following days to ensure that they
120 properly recovered after surgery. Injected mice were assessed for viral expression after a minimum
121 of 3 weeks. All viral constructs were acquired from Vector Core Facilities, Gene Therapy Centre
122 (North Carolina, UNC). Viral constructs used: AAV5-EF1a-DIO-ChR2(H134R)-mCherry, AAV5-EF1a-
123 DIO-ChR2(H134R)-eYFP, AAV-EF1a-DIO-Arch3.0-EYFP, AAV-Ef1a-DIO-hChR2(E123T-T159C)-p2A-
124 mCherry-WPRE (Dr. Karl Deisseroth), and AAV-CAG-FLEX-ArchT-GFP (Dr. Ed Boyden).

125

126 ***Ex vivo* brain slice preparation**

127 Mice were anaesthetised using 4 % isoflurane (Oxford University Veterinary Services) and were
128 sacrificed by decapitation after the pedal reflex was abolished. Brains were extracted in warm (30 -
129 35 °C) sucrose solution (34.5 mM NaCl, 3 mM KCl, 7.4 mM MgSO₄·7H₂O, 150 mM sucrose, 1 mM
130 CaCl₂, 1.25 mM NaH₂PO₄, 25 mM NaHCO₃ and 15 mM glucose) and transverse hippocampal slices
131 of 350 µm thickness were cut using a Leica vibratome (VT 1200S) (Huang et al. 2013). Slices were
132 then immediately placed in an interface storing chamber containing warm (30 - 35 °C) aCSF (126
133 mM NaCl, 3.5 mM KCl, 2 mM MgSO₄·7H₂O, 1.25 mM NaH₂PO₄, 24 mM NaHCO₃, 2 mM CaCl₂ and 10
134 mM glucose) at least one hour to equilibrate. All solutions were bubbled with 95% O₂ and 5% CO₂
135 beginning 30 minutes before the procedure until the end of the experiment.

136

137 **Electrophysiology**

138 Extracellular recordings were conducted in an interface recording chamber at 33-34 °C. Visualisation
139 of the slices and electrode placement was performed using a Wild Heerbrugg dissection microscope.
140 Local field potentials were recorded by inserting a borosilicate glass electrode filled with aCSF (tip
141 resistance = 1 - 5 MΩ) in CA3 pyramidal layer. Data were acquired and amplified (x 10) by Axoclamp
142 2A (Molecular Devices). The signal was further amplified x 100 and low pass filtered at 1 KHz (LPBF-
143 48DG, NPI Electronic). The signal was then digitised at 5 kHz by a data acquisition board (ITC-16,
144 InstruTECH) and recorded from the IgorPro (Wavemetrics). Gamma oscillations were induced by the
145 application of 5 µM carbachol (Cch). The LFP signal was quantified using real-time fast Fourier
146 transform (FFT) analysis and oscillations were detected by a peak in the power spectrum at low -
147 band frequencies (25 - 49 Hz). For unit recordings a linear 16 channel tungsten multi-electrode array
148 (MEA; MicroProbes) was lowered in the CA3 subfield. The array channels had 100 µm spacing to
149 ensure full coverage of the hippocampus. The MEA was mounted on an RHD2132 Amplifier board
150 and connected to the RHD2000 USB Interface Board (Intan Technologies). Data were acquired at a
151 rate of 20 kHz using the RHD2000 rhythm software (Intan Technologies).

152 Intracellular recordings were always conducted in a single submerged chamber (26 - 32 °C) using
153 borosilicate glass pipettes (5-12 MOhm). The signal was acquired through the MultiClamp 700B
154 amplifier (Molecular Devices) and digitised at a rate of 10 kHz by a data acquisition board (ITC-18,
155 InstruTECH) and was then recorded using the Igor Pro 6.37 software. The signals were low pass
156 filtered (Bessel) at 10 kHz for current clamp mode and 3 kHz for voltage clamp (VC) mode. Slice and
157 cell visualisation were achieved using oblique illumination and monitored through a HAMATATSU
158 ORCA - ER digital camera. Filtered white LED (460 +/- 30 nm, 1.53 mW, Thor Labs) via epi-
159 illumination was used to activate channelrhodopsin (ChR2). Filtered white LED (525 +/-20 nm, 1.45
160 mW, Thor Labs) via epi-illumination was used to activate archaerhodopsin (Arch). For a power of 1.5
161 mW, the light intensity in the illuminated area was 3.68 mW / mm². Cell attached recordings were
162 performed in current clamp (IC) mode (Multiclamp software) using glass pipettes filled with aCSF.
163 For whole cell current clamp recordings pipettes were filled with internal solution containing 110
164 mM KGluconate, 40 mM HEPES, 2 mM ATP-Mg, 0.3 mM GTP-NaCl, 4 mM NaCl, (3-4 mg/ml biocytin,
165 Sigma). For whole cell voltage clamp recordings, pipettes were filled with internal solution
166 containing 140 mM Cesium methanesulfonate, 5 mM NaCl, 10 mM HEPES, 0.2 mM EGTA, 2 mM
167 ATP-Mg, 3 mM GTP-Na, 5 mM QX-314, (3-4 mg/ml biocytin). Series resistance compensation was
168 not performed in all cells included for analysis. For perforated patch recordings the tip of the pipette
169 was filled with a KCl-containing solution (150 mM KCl and 10mM HEPES, pH 7.2-7.3; Osmolality 300
170 mOsmol/Kg). The rest of the pipette was filled with the same KCl solution containing 5 µM
171 gramicidin D (1:1000 DMSO dilution, Sigma) and 10 µM Fluorescein (Sigma) to visualise if there was
172 spontaneous rupture of the membrane during patching experiments.

173

174 **Light delivery**

175 For photo-excitation (ChR2) experiments, light illumination was delivered through a fibre optic using
176 a blue LED (470 +/- 20 nm, Thorlabs, M470F3; max power at fibre optic tip = 10 mW). For photo-

177 inhibition (Arch) experiments light illumination was delivered through a fibre optic by a green LED
178 (530 +/- 30 nm, Thorlabs, M530F2; maximum power at fibre optic tip = 4.25 mW) and with an amber
179 LED (595 +/- 20nm, Doric, maximum power at fibre optic tip = 5 mW). LED module output was
180 controlled using the Igor Pro 6.37 software. Laser photo-inhibition experiments were also
181 performed with a green laser (MatchBox series, 532 +/- 0.5 nm, maximum power at fibre optic that
182 was used approx. 40 mW). In these experiments the data were acquired at a rate of 10 kHz using
183 Igor Pro 6.37. The laser was operated manually, and the light duration was recorded using an
184 Arduino Uno board that created a digital time stamp. Experiments were only included if the laser
185 illumination duration was between 19.6 - 20.7 seconds. The area of light illumination was estimated
186 to have a diameter of 1 - 2 mm and therefore for a power of 10 mW the light intensity was between
187 0.8 - 3.2 mW / mm².

188

189 **Histology and imaging**

190 After electrophysiological recordings, acute brain slices were fixed in 4 % PFA overnight. Slices were
191 kept in PBS (Phosphate Buffered Saline: 1.37 mM NaCl, 2.7 mM KCl, 10 mM Na₂HPO₄, 2 mM KH₂PO₄)
192 at 4 °C for short-term storage. For biocytin labelling the slices were washed with 1X PBS 3-4 times
193 and permeabilized with freshly prepared 0.3 %-Triton 1X PBS for 4 - 5 hours. Streptavidin conjugated
194 to Alexa FluorTM 488 (Invitrogen S32355) in PBS-Triton 0.3 % (1:500) was incubated overnight at 4
195 °C. The slices were then washed 4 - 5 times in PBS for 2 hours. Slices were mounted on glass slides
196 using mounting media (DAKO). Confocal images (1024 x 1024) were acquired on a Zeiss LSM700
197 upright confocal microscope using the 10x air objective and digitally captured using the default LSM
198 acquisition software. Pyramidal cell reconstruction was performed on neuron studio and simple
199 neurite tracer plugin on Fiji. Fluorescence expression was quantified using 40 pixel wide line profiles
200 through the layers of CA3 in Fiji, with background subtraction, and the signal normalised to the
201 background.

202

203 **Analysis of local field potentials**

204 In order to characterise and analyse the oscillations, a Hanning window was applied and the power
205 spectra were calculated as the normalised magnitude square of the FFT (Igor Pro 6.37). The 50 Hz
206 and 100 Hz frequencies were not included in the analysis to exclude the mains noise and its
207 harmonic component. The oscillation amplitude was quantified firstly by measuring the peak of the
208 power spectrum termed as peak power and secondly by measuring the area below the power
209 spectrum plot in the gamma-band range (20 - 100 Hz) termed as power-area. The peak frequency
210 of the oscillation was obtained by measuring the frequency at which the peak of the power spectrum
211 occurred in the gamma-band range. In order to quantify when Cch-induced oscillations were
212 abolished upon light stimulation, and to exclude the peak frequencies of those oscillations from
213 further analysis, one of the two criteria had to be met. Firstly, an auto-correlation of the oscillations
214 was computed and was fitted with a Gabor function ($f(x) = (A * \cos(2\pi * f * x)) * e(-x^2 / 2 * \tau)$). The first criterion was met if the resulting Gabor fit had a linear correlation
215 coefficient, $r > 0.7$ and $\sqrt{f * \tau} > 0.1$ (> 0.15 for frequencies higher than 50 Hz). The second
216 criterion was a power-area larger than $125 \mu V^2$ in the range of ± 5 Hz of the peak frequency. The
217 power-area was always included in the analysis even if oscillations were abolished. The power
218 spectrum analysis for *de novo* oscillations was performed in the range of 52 - 149 Hz with the only
219 criterion for oscillation presence being that the power-area in ± 5 Hz of the peak frequency was
220 larger than $40 \mu V^2$. Hilbert transforms were used to obtain instantaneous gamma magnitude for
221 sinusoidal modulation of gamma oscillations (band-pass filtered 20 - 120 Hz). For visualisation
222 purposes the magnitude of the continuous wavelet transform was used normalised by max value
223 (Morlet wavelet; $\omega = 6$).
224

225

226 **Spike detection and analysis**

Unit detection was performed using custom-written procedures in MATLAB (2015-17, Mathworks). Extracellular spikes from the 16 channel MEA were detected as described before by Quiroga and colleagues (Quiroga, Nadasdy & Ben-Shaul, 2004; Quiroga, 2009). Briefly, the MEA data were processed with an elliptical band-pass filter (for spike detection: 4th order, 300 - 3000 Hz, for spike sorting: 2nd order, 300 - 6000 Hz). Spikes were detected as signals exceeding 5 standard deviation (s.d.) of the noise, $5 * \sigma_n$, where $\sigma_n = \text{median} \{|x| / 0.6745\}$. Signals that exceeded 10 times the s.d. of the detected spike amplitudes were eliminated as artefacts/population spikes. Subsequently, spikes that had peaks occurring at the same time (< 0.1 ms) across channels were grouped together as one unit. This prevented detection of the same unit more than once. Clustering of the detected spikes was performed using custom-written procedures in Igor Pro 6.37. A spike sorting procedure adapted from Fee and colleagues was used to explore whether neurons displaying specific spike waveforms were selectively recruited by optogenetic stimulation (Fee, Mitra & Kleinfeld, 1996). Briefly, spike metrics were converted into z scores, over-clustered using an in-built k-means algorithm, and progressively aggregated if the intercluster distance was < 2.5 and merging did not produce more violations of refractory period of 2 ms. Analysis was performed on the clustered spikes, with auto-correlation and cross-correlation plots used to validate the clustering procedure. Spike metrics from the average waveform for each cluster were used to identify different waveform types via a k-means algorithm. This clustering procedure is likely to be conservative, and underestimate the firing rate of individual neurons, but was deemed sufficiently robust to detect any bias in optogenetic recruitment. A single unit cluster was identified if it 1) had less than 1.4 % of its total spike waveforms within 2 ms of its refractory period and 2) consisted of more than 800 members. When a cluster did not obey these criteria, it was merged with other clusters that had similar action potential waveforms giving rise to a multi-unit cluster. Clusters were identified as expressing ChR2 if the spike rate in the first 100 ms of the step stimulus was 3 s.d. above the baseline spike rate. The remaining clusters were classified based on the delay

252 between the negative and positive peaks in the average waveform as fast-spiking (<0.6 ms) or
 253 regular-spiking (>=0.6 ms). The Activation Index was calculated over the last second of the step
 254 stimulus as the difference between the light-induced and baseline spikes rates divided by their sum,
 255 and designed to measure sustained firing. The Theta Modulation Index was calculated as the rank
 256 correlation coefficient between the spike time histogram and the theta-modulated amplitude of the
 257 light stimulus.

258

259 **Computational modelling**

260 The activity in populations of excitatory and PV+ inhibitory neurons were modelled using Wilson-
 261 Cowan firing rate equations (Devalle, Roxin & Montbrió, 2017):

$$262 \quad \tau_m \dot{R} = -\dot{R} + G(D_{syn_total} + D_{ext}) \quad (1)$$

263 where τ_m is the membrane time constant, R is the mean firing rate (and the overdot indicates a
 264 derivative taken with respect to time), D_{syn_total} is the total synaptic drive, D_{ext} is the external drive
 265 to mimic carbachol induced depolarisation or optogenetic manipulation, and $G(x)$ is the population
 266 response function:

267

$$268 \quad G(x) = \frac{1}{\sqrt{2\pi}\tau_m} \cdot \sqrt{x + \sqrt{x^2 + \Delta^2}} \quad (2)$$

269 This includes the parameter Δ to represent heterogeneity, which was set at 0.3 throughout.

270

271 The activity in a population of SST+ interneurons was modelled using macroscopic equations derived
 272 from quadratic integrate-and-fire neurons (Devalle, Roxin & Montbrió, 2017):

273

$$274 \quad \tau_m \dot{R} = \frac{\Delta}{\pi\tau_m} + 2RV \quad (3)$$

275

$$\tau_m \dot{V} = V^2 - (\pi \tau_m R)^2 + D_{syn_total} + D_{ext} \quad (4)$$

which include the influence of mean membrane voltage (V), and enable oscillations in a lumped model of inhibitory neurons. τ_m was 10 ms for excitatory cells, and 5 ms for both populations of inhibitory cell.

For all three neuronal populations, the total synaptic drive was the sum of excitatory and inhibitory inputs each cell population received, with each modelled as exponentially decaying synapses:

$$D_{syn_total} = \sum_i D_{syn_i} \quad (5)$$

$$D_{syn_i} = w_i \tau_m S_i \quad (6)$$

$$\tau_{syn_i} \dot{S}_i = -S_i + R_{pre_i} \quad (7)$$

where w is the synaptic weight (Table 1), S is the variable for synaptic activation, τ_{syn} is the synaptic time constant (Table 1) and R_{pre} is the respective presynaptic spike rate. The relative synaptic weights were based on synaptic currents recorded in excitatory and inhibitory neurons during cholinergically-induced gamma oscillations (Oren *et al.*, 2006). The synaptic time constants were tuned to give ~35 Hz oscillations across a range of I_{ext} in excitatory cells (6-12).

The differential equations were solved in MATLAB 2019a using the ode23tb function and a 0.1 ms time step. The signal used to analyse rhythmic activity was the inhibition in the E cells, calculated as the sum of wS for the input from PV+ and SST+ neurons, as cholinergically-induced LFP oscillations in the hippocampus *ex vivo* appear to reflect inhibitory currents in pyramidal neurons (Mann *et al.*, 2005; Oren, Hájos & Paulsen, 2010). Similar to the analysis of the LFP, the frequency was only

301 reported if, i) the Gabor fit to the auto-correlation showed $r > 0.7$ and $\sqrt{f * \tau} > 0.1$, and ii) the
302 peak power in the gamma range was >1 . The peak power was calculated for all simulations.

303

304 **Statistics**

305 Repeated measures ANOVA (rmANOVA) was performed in SPSS 24 with a Greenhouse-Geisser
306 correction where required (i.e. significance in Mauchly's test for sphericity) and followed by
307 Bonferroni-corrected post-hoc paired t-tests. Linear correlations, circular correlations, and
308 Bonferroni-corrected one sample t-tests were performed using Igor Pro 6.37. Spearman's Rank
309 correlations were performed in SPSS 24. Scatter-bar charts were generated using PRISM 7. Circular
310 statistics of spike phase relative to ongoing oscillations in the LFP were calculated using in-built
311 functions in Igor Pro 6.37. The measurements spiking rates deviated from normality, and were
312 analysed using non-parametric statistical tests performed in SPSS 24: differences between cell types
313 were analysed using Kruskal-Wallis Test, followed by posthoc Dunn's test, with Bonferroni
314 correction for multiple comparisons. Differences across stimulus types (step and theta) were
315 analysed using the Wilcoxon signed rank test, and the significance of modulation indices analysed
316 using the one-sample Wilcoxon signed rank test ($H_0=0$). Error bars in graphs represent the standard
317 error of the mean, unless explicitly stated otherwise. Stars represent significance values where * p
318 <0.05 , ** $p <0.01$ and *** $p <0.001$.

319 **Results**

320 **PV+ interneuron activity is necessary for cholinergically-induced gamma oscillations** 321 **in hippocampal CA3**

322 In order to test if the activity of PV+ interneurons is necessary for the generation of slow
323 hippocampal gamma oscillations, we took advantage of optogenetic photo-inhibition (Chow *et al.*,

2010). We injected PV-cre mice with AAV carrying the inhibitory proton pump archaerhodopsin (Arch3-eYFP or ArchT-GFP). Expression of Arch in PV-cre mice was restricted to the pyramidal cell layer indicating preferential expression in perisomatic targeting PV+ interneurons (Fig. 1A & 2B) (Somogyi & Klausberger, 2005; Royer *et al.*, 2012; Hu, Gan & Jonas, 2014). Intracellular recordings performed in opsin expressing cells demonstrated that these cells were fast-spiking and that sustained light illumination was able to produce robust hyperpolarisation, indicating functional expression of Arch in PV+ interneurons (Fig. 1B&C).

Gamma oscillations were induced in hippocampal slices from PV-Arch mice in area CA3 using bath application of the cholinergic agonist carbachol (Cch - 5 μ M). Local field potential recordings from the CA3 pyramidal cell layer revealed robust gamma oscillations that were centred around 30 – 40 Hz (Fig 1D-F), as has been reported previously (Fisahn *et al.*, 1998; Hájos *et al.*, 2004; Mann *et al.*, 2005). In each optogenetic experiment the photo-excitation protocols were repeated multiple times (4 – 10 trials) and the mean response reported. Overall, sustained photo-inhibition of PV+ interneurons using LED illumination (< 5mW) significantly decreased gamma power area (0.82 ± 0.068 of baseline period, $t = 2.59$, $p = 0.029$, one sample t-test; Fig. 1E&G), although increases in power were observed in some slices (Fig. 1G). A significant suppression was also observed in the period of 0.5 - 1.5 seconds following light illumination termination (0.85 ± 0.022 of baseline period, $t = 6.70$, $p < 0.001$, one sample t-test; Fig. 1G). The light-induced changes in gamma power were reversible, as there were no significant changes in the gamma power area recorded during the baseline periods across trials ($F(4, 116) = 0.68$, $p = 0.61$, rmANOVA). In addition, the changes in gamma power were not accompanied by a consistent alteration in gamma frequency ($F(1.44, 43.23) = 1.25$, $p = 0.288$, rmANOVA; Fig. 1H), although there was a significant correlation between the changes in frequency and power area ($t = 2.77$, $p = 0.01$, Pearson correlation, Fig. 1I), suggesting a consistent modulation of endogenous oscillatory activity.

348 While LED photo-inhibition of PV+ interneurons significantly modulated gamma power, the
349 oscillations did not collapse. Pyramidal neurons make strong recurrent connections with PV+
350 interneurons (Mann, Radcliffe & Paulsen, 2005; Oren *et al.*, 2006; Hofer *et al.*, 2011; Packer & Yuste,
351 2011; Bartos & Elgueta, 2012; Kohus *et al.*, 2016), and it might be hard to break these feedback
352 loops with photo-induced inhibitory currents. To test this possibility, we used long-lasting laser
353 illumination with the prospect of biochemically silencing PV+ interneurons, by preventing synaptic
354 release via terminal alkalisation (El-Gaby *et al.*, 2016). PV+ interneurons expressing ArchT-GFP were
355 illuminated with sustained green laser light (532 nm, approx. 18 mW for 20 seconds). Similar to the
356 LED experiments, there were inconsistent network responses to PV+ interneuron photo-inhibition
357 at the beginning of laser illumination (1.00 +/- 0.087 of baseline period, $t = 0.04$, $p = 1.00$, one sample
358 t-test; Fig. 1J&K). However, the power of the oscillation consistently decreased during sustained
359 laser illumination (0.57 +/- 0.086 of baseline period, $t = 5.00$, $p < 0.001$, one sample t-test; Fig. 1J&K)
360 and remained suppressed in first 10 seconds following laser stimulation (Post1: 0.78 +/- 0.071 of
361 baseline period, $t = 3.17$, $p = 0.030$, one sample t-test; Fig. 1J&K), but eventually recovered (Post2 :
362 0.98 +/- 0.04 of baseline period, $t = 0.43$, $p = 1.00$, one sample t-test; Fig. 1J&K). There was no
363 consistent effect on the frequency of the oscillations ($F(1.93, 23.21) = 7.29$, $p = 0.004$, rmANOVA;
364 paired t-tests to baseline, $t < 2.692$, $p > 0.078$, Fig. 1J&L). Laser illumination of PV+ interneurons
365 expressing only control fluorophore did not alter gamma oscillation power nor frequency (data not
366 shown). This slow and selective process of decreasing gamma power is consistent with biochemical
367 silencing of synaptic terminals (El-Gaby *et al.*, 2016). These results further support the importance
368 of PV+ interneuron activity in generating gamma oscillations in hippocampal area CA3 (Hájos *et al.*,
369 2004; Mann *et al.*, 2005; Gulyás *et al.*, 2010; Tukker *et al.*, 2013). Residual gamma oscillations
370 following photo-inhibition of PV+ interneurons may reflect incomplete transfection of the PV+
371 network or the presence of a distinct oscillatory circuit.

372

373 **SST+ interneurons are necessary for Cch-induced gamma oscillations in** 374 **hippocampal area CA3**

375 To examine if SST+ interneuron activity is also required during Cch-induced gamma oscillations in
376 CA3, we injected the AAV-Arch vector (Arch3-eYFP or ArchT-GFP) intrahippocampally in SST-cre
377 mice. Expression of Arch was restricted to the strata oriens, radiatum and lacunosum moleculare
378 (Fig. 2A&B), suggesting expression in SST+ dendrite-targeting interneurons (Ma *et al.*, 2006; Lovett-
379 Barron *et al.*, 2012; Muller & Remy, 2014; Urban-Ciecko & Barth, 2016). Whole-cell recordings were
380 performed in opsin positive cells and indicated functional expression of Arch (n = 4, Fig. 2C&D). SST+
381 interneurons often showed a pronounced sag during current- and light-induced hyperpolarisation
382 (Fig. 2C&D), and could show rebound spikes following light pulses and steps (data not shown), but
383 remained hyperpolarised throughout photo-stimulation.

384 Unlike the experiments with PV+ photo-inhibition, sustained photo-inhibition of SST+ interneurons
385 using LED illumination (< 5mW) reliably decreased gamma oscillation power (0.69 ± 0.057 of
386 baseline period, $t = 5.40$, $p < 0.001$, one sample t-test; Fig. 2E-G), which remained suppressed in the
387 immediate period following SST+ interneuron photo-inhibition (0.76 ± 0.039 of baseline period, t
388 $= -6.26745$, $p < 0.001$, one sample t-test; Fig. 2G). This post-light suppression was reversed from
389 trial to trial ($F(4, 164) = 2046$, $p = 0.048$, rmANOVA; all paired t-tests $t > 2.81$, $p > 0.07$). In addition,
390 light stimulation significantly modulated oscillation frequency ($F(1.25, 39.97) = 22.60$, $p < 0.001$,
391 rmANOVA), with an increase in frequency from 37.79 ± 1.083 Hz to 43.00 ± 1.466 Hz during light
392 stimulation ($t = 4.74$, $p < 0.001$, paired t-test), which reversed following light offset (Fig. 2H). There
393 was also a significant correlation between the changes in frequency and power area of the
394 oscillations ($t = 3.11$, $p = 0.004$, Pearson correlation, Fig. 2I), suggesting again a consistent
395 modulation of endogenous oscillatory activity.

396 In the first 10 s of stronger laser illumination (532 nm, approx. 18 mW, 20 s total duration) similar
 397 effects were observed as in the LED experiment. Specifically, the power of Cch gamma oscillations
 398 decreased (0.70 ± 0.064 of baseline, $t = 4.76$, $p < 0.001$, one-sample t-test), and the peak frequency
 399 increased (34.22 ± 1.191 Hz to 38.60 ± 1.868 Hz, $t = 3.93$, $p = 0.011$, paired t-test; rmANOVA,
 400 $F(1.79, 17.87) = 4.61$, $p = 0.028$; Fig. 2J-L). During the second half of the stimulation period (10 - 20
 401 s), gamma power was strongly suppressed (0.35 ± 0.090 of baseline, $t = 7.23$, $p < 0.001$, one sample
 402 t-test; Fig. 2J-L), often resulting in oscillation collapse (7/13 slices). This could indicate that silencing
 403 SST+ interneurons is sufficient to disrupt the hippocampal network during gamma oscillations and
 404 that SST+ interneuron activity is necessary for proper maintenance of Cch-induced oscillations in
 405 the CA3 area of the hippocampus. Moreover, the robust upregulation of gamma oscillation peak
 406 frequency (Fig. 2J&L) suggests that SST+ interneurons can exert strong control over the frequency
 407 of slow gamma oscillations.

408

409 **Rhythmic synchronisation of the hippocampal network by perisomatic** 410 **and dendritic inhibition**

411 The experiments using photo-inhibition indicate that the generation of gamma oscillations in
 412 hippocampal area CA3 involves the endogenous recruitment of both PV+ and SST+ interneurons. In
 413 order to test whether the activation of PV+ or SST+ interneurons is sufficient to entrain the
 414 hippocampal network at gamma frequencies, we next examined cell type-specific photo-excitation
 415 using Channelrhodopsin 2 (ChR2) (Nagel *et al.*, 2003; Boyden *et al.*, 2005). Injection of AAV-ChR2-
 416 mCherry produced similar expression patterns as Arch in both PV- and SST-Cre mouse lines (Fig.
 417 3A&B). Photo-excitation of ChR2-expressing PV+ interneurons at 40 Hz (1-5 ms pulse width) reliably
 418 evoked spikes throughout pulse trains (median spike rate [interquartile range (IQR)] = 40.5 [40.3,
 419 43.3] Hz; median spike fidelity [IQR] = 1.0 [1.0, 1.0]; $n=5$; Fig. 3C&D), and entrained ongoing

oscillations in 14/18 experiments ($>2\text{mW}$; $n = 12$ at 5.5 mW , $n = 6$ at 2.2 mW - merged due to similar effects; Fig. 3E,G&I). In the remaining 4 out of 18 experiments the ongoing oscillations were not entrained (Fig. 3J). This effect was likely observed due to low ChR2 expression, as pulses with longer width (5 ms) entrained the oscillation in the same experiments (Fig. 3J). Thus, PV+ interneurons are sufficient to synchronise the hippocampal network at gamma frequencies.

Rhythmic photo-excitation of SST+ interneurons evoked spikes throughout pulse trains (median spike rate [IQR] = $41.7 [40.4, 71.3]$ Hz; median spike fidelity [IQR] = $1.0 [1.0, 1.0]$; $n=13$; Fig. 3C&D). This stimulation pattern reliably entrained ongoing oscillations in 19 out of 22 experiments ($>2\text{mW}$; $n = 13$ at 5.5 mW , $n = 9$ at 2.2 mW - merged due to similar effects; Fig. 3F,H&K). In the remaining 3 out of 22 experiments, oscillations were abolished during 40 Hz photo-excitation. These results indicate that transient activation of SST+ dendrite-targeting interneurons is also sufficient to synchronise the hippocampal network at gamma frequencies. Activation of PV+ and SST+ interneurons produced opposite deflections in the pulse-locked waveform of the LFP recorded in the stratum pyramidale (Fig. 3E-H), as might be expected from the somatodendritic profile of their axon terminations. However, activation of SST+ interneurons was sometimes accompanied by an initial fast negative component (Fig. 3H), which was reminiscent of a population spike arising from the synchronised firing of excitatory cells in the hippocampus (Andersen, Bliss & Skrede, 1971; Wierenga & Wadman, 2003), despite the sparsity of SST+ axons in this layer.

To study the SST+ induced waveform in isolation, we repeated the same experiment in quiescent slices, perfused only with aCSF. Blue light pulses (1 ms width) at 40 Hz induced strong pulse-locked field responses with fast-negative deflections, which were resistant to glutamate receptor blockers (Fig. 4A-C), but were followed by a glutamate receptor-mediated positive deflection. Application of GABA_A receptor (GABA_AR) blockers reduced the overall amplitude of the phase-locked field responses ($n = 3$; Fig 4D-E). Furthermore, application of GABA_AR blockers lead to light-induced

444 epileptiform bursts ($n = 4$; Fig. 4F) during 2 s sustained photo-excitation. These results suggest that
445 SST+ interneuron photo-excitation generates network excitation, that is not mediated through
446 GABA_ARs, at the onset of light illumination. We did not observe ChR2 expression in CA3 pyramidal
447 neurons during whole cell recordings, but they did receive weak excitatory postsynaptic currents
448 (EPSCs) throughout light illumination (Fig 4G). Light-evoked inhibitory postsynaptic currents current
449 (IPSCs) were always larger than evoked EPSCs, and perforated patch-clamp recordings in current-
450 clamp mode revealed that pyramidal cells were inhibited during SST+ interneuron photo-excitation
451 ($n = 18$, Fig. 4G-I). Activation of GABA_BR may contribute to the dominant effect of membrane
452 hyperpolarisation, as these receptors were blocked by QX-314 during voltage-clamp recordings.
453 However, this does suggest that there are some off-target effects in slices from SST-ChR2 mice.

454

455 **Sustained activation of PV+ interneurons suppresses Cch-induced gamma** 456 **oscillations**

457 We used two patterns of sustained activation in slices from PV-ChR2 mice: light steps to drive tonic
458 firing and fully-modulated sine waves at 8 Hz to mimic excitatory input during theta-frequency
459 oscillations (Buzsáki, 2002). In a subset of light step experiments, we recorded ongoing gamma
460 oscillations in the LFP whilst tonically driving PV+ interneurons at increasing strengths across trials
461 (by changing the levels of blue light illumination, 10 - 5500 μ W). The change in power between
462 baseline and light activation period was measured at each light intensity level. We then obtained
463 the response level at which the power changed by half of the maximum for each experiment (half-
464 maximal response). For half-maximal response trials, photo-excitation of PV+ interneurons (2
465 seconds) consistently decreased the power-area (0.52 ± 0.016 compared to baseline, $t = -29.56$, p
466 < 0.001 , one-sample t-test; Fig. 5A-C & E) and increased the peak frequency (from 32.70 ± 0.793

467 Hz (baseline) to 38.76 ± 1.094 Hz, $t = 8.21$, $p < 0.001$, paired t-test; Fig. 5D&F). Furthermore, there
 468 was a progressive decrease in power ($r = -0.84$, $n = 121$ values, $t = 17.00$, $p < 0.001$; Fig. 5G) and
 469 increase in frequency ($r = 0.49$, $n = 100/121$ values, $t = 5.60$, $p < 0.001$; Fig. 5H) as the light intensity
 470 increased. In order to estimate the maximal effect of PV+ interneuron stimulation, we pooled
 471 experiments using strong light intensity illumination (> 2 mW, including cases where light intensity-
 472 response curves were not assessed; $n = 14$ at 5.5 mW, $n = 9$ at 2.2 mW). Overall, strong light
 473 illumination caused a substantial decrease in the normalised power-area (0.09 ± 0.029 , $t = 31.07$
 474 $p < 0.001$, one-sample t-test; Fig. 5I&J) and abolished the oscillations in most experiments (17/23).
 475 These results indicate that progressive up-regulation of PV+ interneuron activity decreases gamma
 476 power and increases the frequency until the rest of the hippocampal network is fully silenced.

477 Interneurons have been shown to be particularly susceptible to depolarisation block (Herman *et al.*,
 478 2014), and we did observe this in one of the current-clamp recordings from PV+ interneurons during
 479 step illumination (median spike rate [IQR] = $30.6 [8.4, 91.1]$ Hz; $n = 6$; excluding 1 neuron showing
 480 depolarisation block). This seems unlikely to explain the effects we observe, as photo-stimulation in
 481 aCSF did not induce increases in network activity (Fig. 5K&L). In order to examine directly whether
 482 PV+ interneurons could maintain spiking with sustained photo-excitation during Cch-induced
 483 oscillations, we recorded spiking activity using a linear multi-electrode array (MEA) (Fig. 6A). PV+
 484 interneurons (spike width: 0.49 ± 0.04 ms) showed variability in spike rates (median spike rate
 485 [IQR] = $44.5 [17.3, 108.8]$ Hz; $n = 18$), but this activity was maintained during sustained illumination
 486 (5.5 mW; Median sustained activation index [IQR] = $0.87 [0.46, 1]$, $Z=171$, $p<0.001$, $n=18$, one-
 487 sample Wilcoxon signed rank test; analysis performed on last second of trial), and was associated
 488 with decreased activity of regular spiking [(RS; $-0.72 [-0.92, -0.40]$; $Z=2$, $p<0.001$, $n=53$, one-sample
 489 Wilcoxon signed rank test; $z=65.7$, $p<0.001$ cf. PV+ interneurons, Kruskal-Wallis Test followed by
 490 posthoc Dunn's test with Bonferroni correction for multiple comparisons) and fast-spiking cells (FS;
 491 $-0.52 [-0.82, -0.12]$; $Z=141$ $p<0.001$, $n=49$, one-sample Wilcoxon signed rank test; $z=50.1$, $p<0.001$

492 cf. PV+ interneurons, Kruskal-Wallis Test followed by posthoc Dunn's test with Bonferroni correction
 493 for multiple comparisons)] (Fig. 6B-D&G). Current-clamp recordings from putative pyramidal
 494 neurons confirmed that light stimulation produced sustained membrane hyperpolarisation (Fig. 6I).
 495 These results are consistent with increased PV+ interneuron activity during light illumination that
 496 leads to reduced activity in hippocampal principal cells.

497 During 8 Hz sinusoidal modulation of PV+ interneurons, the instantaneous gamma magnitude,
 498 assessed using the Hilbert transform, was found to be negatively correlated with light intensity in
 499 agreement to light step experiments (across all experiments, Pearson correlation, mean $r = -0.51 \pm$
 500 0.04 , $t > 23.2$, $p < 0.001$, $n = 12$) (Fig. 6H). During MEA recordings, spike rates of PV+ interneurons
 501 correlated positively with theta-frequency changes in light intensity (Median rank correlation
 502 coefficient [IQR] = 0.75 [0.55 , 0.83], $Z=120$, $p=0.001$, $n=15$, one-sample Wilcoxon signed rank test),
 503 while negative correlations were found for the spike rates of RS (-0.19 [-0.37 , -0.09]; $Z=100$, $p<0.001$,
 504 $n=43$, one-sample Wilcoxon signed rank test; $z=48.3$, $p<0.001$ cf. PV+ interneurons, Kruskal-Wallis
 505 Test followed by posthoc Dunn's test with Bonferroni correction for multiple comparisons) and FS
 506 cells (-0.19 [-0.39 , -0.01]; $Z=232$, $p=0.006$, $n=42$, one-sample Wilcoxon signed rank test; $z=45.7$,
 507 $p<0.001$ cf. PV+ interneurons, Kruskal-Wallis Test followed by posthoc Dunn's test with Bonferroni
 508 correction for multiple comparisons) (Fig. 6E). All PV+ interneurons recorded during ongoing slow
 509 gamma oscillations showed significant phase-coupling ($p<0.05$, Rayleigh test), with a mean spike
 510 phase of -1.8 [-2.3 , -0.9] radians (second-order mean [95% confidence intervals]; $n=10$; Fig. 7F&G).
 511 The PV+ interneurons fired at a significantly later phase of the oscillation than the RS cells ($F(2,55)$
 512 $= 5.36$, $p = 0.007$, Two-sample Hotelling test). These findings indicate that PV+ interneurons are
 513 synchronised within slow gamma, and that a transient increase in PV+ interneuron activity causes a
 514 rapid and reversible decrease in the power of the Cch-gamma oscillations and firing rates of other
 515 neurons.

516

517 **Sustained activation of SST+ interneurons induces fast gamma** 518 **oscillations**

519 We obtained the light intensity response curves with light steps in slices from SST-ChR2 mice and
520 observed similar results as in PV-ChR2 experiments. Sustained light illumination decreased the
521 power (0.49 ± 0.029 , $t = 17.53$, $p < 0.001$, one sample t-test; Fig. 7A-C & E) and increased the
522 frequency at half-maximal response (from 34.08 ± 0.954 Hz during baseline period to $38.17 \pm$
523 1.400 Hz, $t = 3.658$, $p < 0.01$, paired t-test; Fig. 7D&F). Moreover, as the light intensity increased, the
524 power progressively decreased ($r = -0.66$, $n = 107$ values, $t = 9.11$, $p < 0.001$; Fig. 7G), and frequency
525 progressively increased ($r = 0.71$, $n = 56$ out of 107 values, $t = 7.41$, $p < 0.001$; Fig. 7H). It is perhaps
526 not surprising that excitatory networks can be suppressed by photo-excitation of GABAergic
527 interneurons. However, different responses were revealed when we assessed the effects of strong
528 photo-excitation of SST+ interneurons on Cch-induced gamma oscillations (light-intensity response
529 curves were performed in a subset of experiments; $n = 18$ slices at 5.5 mW and $n = 13$ slices at 2.2
530 mW, merged). Similar to PV-ChR2 step experiments, the gamma power was reduced during light
531 stimulation when compared to baseline period (0.34 ± 0.150 , $t = -4.39$, $p < 0.001$, one sample t-
532 test; Fig. 7I&J) and in approximately half of the experiments, gamma oscillations were fully abolished
533 ($n = 16/31$ slices). In contrast, in experiments where the oscillations persisted, their frequency
534 increased strongly from 34.63 ± 0.836 Hz during baseline to 62.75 ± 4.921 Hz during light
535 illumination ($n = 15/31$ slices; $t = 5.61$, $p < 0.001$, paired t-test; Fig 7I-K). These fast gamma oscillations
536 occurred most reliably in slices for which the light-intensity response curves were not obtained. In
537 order to test if SST+ interneuron photo-excitation alone is sufficient to induce oscillations, as
538 opposed to simply increasing the frequency of ongoing activity, we repeated the same experiments
539 in the absence of Cch. Sustained photo-excitation of SST+ interneurons induced *de novo* oscillations

540 in the fast gamma-band range with peak frequency of 80.5 ± 2.48 Hz (12/16 slices; Fig. 8A,C&D).
 541 Isolating the CA3 area from DG did not prevent the generation of *de novo* oscillations ($n = 3$ slices).
 542 Furthermore, sinusoidal light activation at 8 Hz (theta photo-excitation) also induced robust
 543 oscillations with higher peak frequency than the tonic activation 111.2 ± 3.15 Hz (13/17 slices; $t =$
 544 7.64 , $p < 0.001$, two-sample t-test; Fig. 8B-D). This is consistent with previous experiments showing
 545 that transient light activation induces higher frequency oscillations than sustained illumination
 546 (Butler *et al.*, 2016; Betterton *et al.*, 2017). Furthermore, the power ($r = 0.67$, $n = 70$ values, $t = 7.52$
 547 $p < 0.001$) and frequency ($r = 0.77$, $n = 48/70$ values, $t = 8.20$, $p < 0.001$) of the *de novo* oscillations
 548 progressively increased as the light intensity of theta photo-excitation was elevated (Fig. 8E&F). This
 549 monotonic increase in peak frequency contrasts with the properties of oscillations induced by
 550 photo-excitation of principal cells in the hippocampus, where the frequency of the oscillations
 551 remains relatively constant within the slow gamma band across light intensities (Butler *et al.*, 2016;
 552 Betterton *et al.*, 2017; Butler, Hay & Paulsen, 2018). Therefore, SST+ interneuron photo-excitation
 553 in CA3 appears to induce a distinct type of gamma activity.

554 The fast gamma oscillations that emerge during sustained photo-excitation of SST+ interneurons
 555 could reflect the intrinsic synchronisation of SST+ networks, but there are a number of possible
 556 scenarios in which this stimulation paradigm could lead to the activation of other hippocampal
 557 microcircuits involving network excitation. Depolarising GABA could contribute to recruitment of
 558 postsynaptic targets, but perforated patch recordings from hippocampal cells in stratum pyramidale
 559 (aCSF only) showed that they were hyperpolarized by light illumination (Fig. 4H&I). Alternatively,
 560 network excitation and oscillogenesis could emerge following depolarisation block of SST+
 561 interneurons, and subsequent disinhibition, but direct photo-inhibition of SST+ interneurons was
 562 not able to generate *de novo* oscillations (Fig. 7L&M). However, the power of the light-induced
 563 oscillations was markedly reduced following block of either fast excitation or inhibition (Fig. 8G&H).

564 This suggests that the light-induced oscillations recorded in LFP do not emerge solely from the
565 GABAergic activity of SST+ interneurons.

566 Current-clamp recordings from SST+ interneurons during step illumination revealed that
567 depolarisation block was quite common in these cells that were located close to the surface (median
568 spike rate [IQR] = 43.8 [33.4, 75.7] Hz; n = 8; excluding 7 showing depolarisation block). To directly
569 test if photo-excitation of SST+ interneurons leads to a dominant effect of depolarisation block
570 during ongoing gamma oscillations, and whether photo-excitation is associated with net increases
571 or decreases in the spiking activity of other neurons in the network, we performed MEA recordings
572 (Fig. 8I-M). We found that SST+ interneurons (spike width: 0.69 +/- 0.03 ms) displayed robust
573 activation (median spike rate [IQR] = 49.2 [29.5, 79.8] Hz; n = 68) that was sustained throughout the
574 course of step stimulation (Median sustained activation index [IQR] = 0.90 [0.76, 0.98], Z=2346,
575 p<0.001, n=68, one-sample Wilcoxon signed rank test; Fig. 8I,J&M), and faithfully followed the 8 Hz
576 sine stimulation (Median rank correlation coefficient [IQR] = 0.63 [0.52, 0.72], Z=1484, P<0.001,
577 n=54, one-sample Wilcoxon signed rank test; Fig. 8K&M). All but 3 of the SST+ interneurons
578 recorded were significantly phase-coupled to the induced fast gamma-frequency oscillations
579 (p<0.05, Rayleigh test), with a mean spike phase of -2.0 [-2.1, -1.8] radians (second-order mean [95%
580 confidence intervals]; n=65; Fig. 8L,M). The RS and FS cells showed significantly weaker modulation
581 (Fig. 8J,K), but did not appear to be suppressed as in the PV-ChR2 experiments, and rather showed
582 an insignificant trends towards both increased activity during step illumination (Median sustained
583 activation index [IQR]; RS: 0.12 [-0.08, 0.54], Z=50, p=0.13, n=11; FS: 0.49 [-0.14, 0.59], Z=24, p=0.09,
584 n=7; one-sample Wilcoxon signed rank tests) and positive correlations with theta-frequency
585 changes in light intensity (Median rank correlation coefficient [IQR]; RS: 0.26 [-0.07, 0.53], Z=49,
586 p=0.16, n=11; FS: 0.28 [0.09, 0.57] (Z=25, p=0.06, n=7, one-sample Wilcoxon signed rank tests). The
587 majority of RS (8/11) and FS cells (4/7) were also significantly phase-coupled to the light-induced
588 fast gamma oscillations (p<0.05, Rayleigh test), but did not show a consistent mean firing phase (RS:

589 $F(2,8)=2.3$, $p=0.18$; FS: $F(2,2)=4.5$, $p=0.19$; parametric second-order analysis (Zar, 1999)) (Fig. 8L,M).
590 Overall, this suggests that the dominant change in the network during the induction of fast gamma
591 oscillations is a robust increase in the spiking of SST+ interneurons.

592 To explore whether the recruitment of SST+ interneurons might differ between step and theta
593 stimulation, we analysed the maximum spike rates in the second half of the stimulation trials (20
594 ms bins). The maximum spike rates during theta stimulation were significantly higher than during
595 the step stimulation ($Z=148$, $p<0.001$, $n=54$; Wilcoxon signed rank test). As theta stimulation induced
596 faster gamma oscillations than step stimulation (see Fig. 8D), this further suggests that the
597 frequency of fast gamma oscillations depends on the overall levels of SST+ interneuron excitation.

598

599 **Computational model of hippocampal gamma oscillations including PV+** 600 **and SST+ interneurons**

601 In order to provide mechanistic insight into how optogenetic manipulation of PV+ and SST+
602 interneurons impact hippocampal network dynamics, we developed a mean firing rate model
603 including these two interneuronal subtypes. It has previously been shown that gamma oscillations
604 in hippocampal CA3 can be modelled using Wilson-Cowan equations in an excitatory-inhibitory
605 feedback loop (Akam *et al.*, 2012). We therefore used these equations to model the excitatory
606 pyramidal cell (E) and inhibitory PV+ interneuron populations. The activity in the population of SST+
607 interneurons was represented using equations derived from quadratic integrate-and-fire neurons
608 (Devalle, Roxin & Montbrió, 2017), which enables oscillations within a mean firing rate model of an
609 inhibitory network. Both interneuronal subtypes were reciprocally connected with E cells, but not
610 with each other (Fig. 9A), with stronger excitatory connections to PV+ interneurons (Oren *et al.*,
611 2006), and faster synaptic time constants in the E-PV+ loop (see Table 1). Moderate excitatory drive

612 to the E population ($D_{ext} = 6-12$; increments of 1) was sufficient to induce gamma-frequency network
 613 oscillations (30-35 Hz; Fig. 9B), with little change in frequency with increasing drive (see Fig. 9C, for
 614 $\Delta PV+$ drive = 0 or $\Delta SST+$ drive = 0), consistent with the effects optogenetic activation of CA3
 615 pyramidal neurons *ex vivo* (Butler, Hay & Paulsen, 2018). As expected from the synaptic connectivity
 616 and time constants implemented in the network, peak activity occurred first in the E cells, followed
 617 by the PV+ cells (3.7-3.9 ms) and then SST+ cells (4.4-9.9 ms; decreased monotonically with
 618 increasing E drive). This is consistent with the spike delays observed for perisomatic- and dendritic-
 619 targeting interneurons recorded during Cch-induced gamma-frequency oscillations *ex vivo* (Hájos *et al.*, 2004). Oscillations were also observed at higher levels of drive to the E cells ($D_{ext} > 12$), but the
 620 peak in SST+ activity began to precede the peak in PV+ activity, due to the voltage-dependent
 621 acceleration of SST+ activation. The effects of manipulating interneuronal drive were thus examined
 622 across the range of conditions that appeared to best approximate the activity in *ex vivo* slices (E
 623 cells: $D_{ext} = 6-12$).

625 To mimic the effects of optogenetic manipulation using LEDs, a select interneuronal population
 626 received step changes in external drive (2 s), which varied from -10 to +10 across trials, with
 627 increments of 0.2. Moderate inhibition of the PV+ cells (PV cells: $D_{ext} = -0.2$ to -5.4) was ineffective
 628 at silencing PV+ cells and abolishing oscillations (Fig. 9B-D), due to corresponding increases in
 629 recurrent excitation. However, the increases in the firing rates of E and SST+ did have variable effects
 630 on network dynamics. Under some conditions, the increased activity in the slower E-SST+ loop
 631 reduced the frequency of network oscillations (Fig 9C). However, the delay between E and SST+
 632 activity decreased with increasing activation (Fig. 9E), which tended to increase oscillation
 633 frequency, and so increases or decreases in oscillation frequency were observed depending on the
 634 initial conditions and degree of PV+ photo-inhibition (Fig 9C&D). Progressively stronger inhibition of
 635 PV+ cells was capable of at first disrupting rhythmicity, and eventually allowing sufficient
 636 disinhibition of E cells to trigger fast rhythmic activity in the SST+ cells (Fig. 9C&D). In contrast,

637 excitation of PV+ cells readily silenced E cells, and thereby abolished oscillatory activity (Fig. 9B-D).
638 These manipulations of PV+ cells had variable effects on oscillation frequency, but there was a
639 significant negative correlation between peak frequency and peak power for both inhibition
640 (Spearman's $\rho = -0.48$, $n = 288$, $p < 0.001$) and excitation (Spearman's $\rho = -0.55$, $n = 66$, $p <$
641 0.001).

642 To examine the effects biochemically silencing presynaptic PV+ terminals, we included a light-
643 induced reduction in the strength of PV+ connections to E cells and themselves, with a maximum
644 reduction of 50%, an onset time constant of 18.4 s, and recovery time constant of 13.1 s (El-Gaby *et*
645 *al.*, 2016). When combined with presynaptic silencing, a moderate inhibitory drive to PV+ cells (D_{ext}
646 $= -5$) was sufficient to gradually reduce the amplitude of gamma-frequency oscillations over time,
647 and eventually abolish rhythmic activity (Fig. 9F).

648 Applying an inhibitory drive to SST+ cells effectively silenced this population, due to weaker
649 feedback excitation, with a predominant effect of reducing the peak power of gamma-frequency
650 oscillations (Fig. 9B&C). For low levels of inhibition of SST+ cells (SST+ cells: $D_{ext} = -0.2$ to -2) there
651 were variable effects on oscillation frequency, but stronger inhibition either produced a small but
652 consistent increase in frequency (3.0 [2.2, 3.2] Hz; E cells: $D_{ext} = 6$ to 11) or abolished the oscillation
653 (E cells: $D_{ext} = 11$ to 12), depending on the initial conditions (Fig. 9C&D). An increase in frequency of
654 persistent oscillations was expected, as the slower synaptic time constants in the loop between E
655 and SST+ cells tends to lengthen the cycle period, and there was a significant negative correlation
656 between peak frequency and peak power (Spearman's $\rho = -0.28$, $n = 274$, $p < 0.001$). Combining
657 inhibitory drive with presynaptic silencing gradually abolished the oscillation (Fig. 9F).

658 Excitation of SST+ cells also reduced the peak power of gamma-frequency oscillations (Fig. 9C), with
659 corresponding changes in frequency best characterised into 3 phases with increasing drive: 1) the
660 delay in the peak activity of E and SST+ cells decreased (Fig. 9E), increasing oscillation frequency, 2)

661 the increased activity of SST+ cells silenced E cells, abolishing oscillatory activity, and 3) the activity
662 in SST+ cells reached sufficient levels to support intrinsic fast gamma-frequency oscillations (Fig.
663 9C&D). Under some conditions there were intermediate phases, such as a drop in frequency due to
664 doublet spikes in SST+ activity on each cycle (E cells: $D_{ext} = 11$ to 12; SST+ cells: $D_{ext} = 2.8$ to 3.4).
665 Overall, there was a significant negative correlation between peak power and oscillation frequency
666 (Spearman's $\rho = -0.33$, $n = 326$, $p < 0.001$). This computational model of hippocampal oscillations
667 indicates that SST+ interneuron sustained excitation is sufficient to generate gamma oscillations
668 under certain conditions.

669

670 **Discussion**

671 Gamma oscillations depend on synchronised synaptic inhibition, and there is a wealth of evidence
672 suggesting that perisomatic-targeting PV+ interneurons are critical for both current and rhythm
673 generation (Mann *et al.*, 2005; Bartos, Vida & Jonas, 2007; Oren, Hájos & Paulsen, 2010; Tukker *et*
674 *al.*, 2013; Cardin, 2016; Sohal, 2016; Penttonen *et al.*, 1998). Here, we used optogenetic
675 manipulation of PV+ and SST+ interneurons to explore whether PV+ interneurons have a selective
676 role in gamma rhythmogenesis in the hippocampal CA3 *ex vivo*. Our findings suggest that disrupting
677 interneuronal activity, via either photo-inhibition or photo-excitation, generally leads to a decrease
678 in the power and increase in the frequency of ongoing cholinergically-induced slow gamma
679 oscillations. This suggests that both PV+ and SST+ interneurons play key roles in maintaining slow
680 gamma oscillations, and the key differences were that (i) gamma oscillations were more readily
681 disrupted by photo-inhibition of SST+ rather than PV+ interneurons, (ii) manipulation of SST+
682 interneurons modulated gamma frequency more robustly than that of PV+ interneurons, and (iii)
683 photo-excitation of SST+ interneurons could also induce *de novo* fast gamma oscillations. These key

684 differences were replicated in a mean firing rate model, in which excitatory neurons and PV+
685 interneurons were connected in a strong and fast feedback loop, and modelled using Wilson-Cowan
686 equations, and SST+ neurons were modelled using equations derived from quadratic integrate-and-
687 fire neurons that support interneuronal network oscillations.

688 Slow gamma oscillations in the hippocampal CA3 appear to be generated by synaptic feedback loops
689 between excitatory pyramidal neurons and perisomatic-targeting interneurons, both in brain slices
690 (Fisahn *et al.*, 1998; Hájos *et al.*, 2004; Mann *et al.*, 2005; Oren *et al.*, 2006; Butler, Hay & Paulsen,
691 2018) and *in vivo* (Bragin *et al.*, 1995; Csicsvari *et al.*, 2003; Fuchs *et al.*, 2007). In such feedback
692 loops, the period of the oscillation largely reflects the effective time course of inhibitory
693 postsynaptic potentials in the pyramidal cells, which should become shorter with smaller compound
694 inhibitory synaptic currents and/or increased pyramidal cell excitability. The amplitude of the
695 oscillation recorded in the LFP also reflects the amplitude of phasic inhibitory currents in pyramidal
696 neurons (Mann *et al.*, 2005; Oren, Hájos & Paulsen, 2010), and during spontaneous gamma
697 oscillations there is a strong correlation between the instantaneous period and amplitude of each
698 gamma cycle (Atallah & Scanziani, 2009). One might thus expect disinhibition to decrease the
699 amplitude and increase the frequency of gamma oscillations, which is largely what we observed
700 with photo-inhibition of either PV+ or SST+ interneurons.

701 While photo-inhibition of SST+ interneurons was able to reliably disrupt gamma oscillations, it was
702 necessary to use high-powered laser illumination of PV+ interneurons to consistently reduce gamma
703 power, and the oscillations were not abolished under our stimulation paradigms. This is not
704 inconsistent with PV+ interneurons playing a key role in the synaptic feedback loops generating
705 gamma oscillations in the hippocampal CA3, as such a microcircuit should resist disinhibition.
706 Indeed, it appears that strong laser illumination was necessary to biochemically silence PV+
707 interneuron terminals (El-Gaby *et al.*, 2016), and thus break this feedback loop.

708 Our computational model supports these conclusions, and provides insight into a potential
709 mechanism for the network effects of photo-inhibition. In this model, the E and PV+ cells are
710 connected in a strong and fast feedback loop, which can oscillate alone at 60-70 Hz with external
711 excitatory drive to the E cells (data not shown). The connections from E cells to SST+ cells are weaker
712 and slower, and recurrent inhibition also has a slower time constant. Under baseline conditions, this
713 loop slows the frequency of network oscillations to 30-35 Hz. However, as the SST+ population is
714 modelled by macroscopic equations for quadratic integrate-and-fire neurons, membrane
715 depolarization leads to sharp increases in firing rate, and can lead to the generation of fast gamma
716 within the SST+ population. Photo-inhibition of SST+ cells reduces the influence of the slow E-SST+
717 loop, while increasing the firing rates of E and PV+ cells, leading to faster and weaker oscillations.
718 Photo-inhibition of PV+ cell firing rates is resisted by strong feedback excitation, but leads to
719 increased activity of E cells, and greater synaptic excitation of SST+ cells. Depending on the initial
720 conditions, this leads to increases or decreases in the oscillation frequency, which may explain the
721 variable effects we observed *ex vivo*. It was possible to break the feedback loop by providing strong
722 inhibitory drive to the PV+ cell population, which could unleash fast gamma in the SST+ cell
723 population. We did not observe such effects *ex vivo*, which could reflect the power of the
724 optogenetic inhibitors and/or light penetration. However, combining more moderate inhibition with
725 presynaptic silencing was also effective in the model.

726 In *ex vivo* brain slices, we also found that photo-excitation of PV+ or SST+ interneurons led to an
727 increase in frequency and decrease in power of gamma oscillations. This might be somewhat more
728 surprising, but our model provides a relatively simple explanation. Photo-excitation of PV+ cells
729 reduces E cell activity and the recruitment of SST+ cells, while photo-excitation of SST+ cells enables
730 their accelerated recruitment due to membrane depolarization. Both of these effects reduce the
731 slowing influence of E-SST+ loop observed during baseline conditions.

732 It was recently suggested that SST+ interneurons, but not PV+ interneurons, contribute to the
733 generation of slow gamma oscillations in V1 (Chen *et al.*, 2017; Veit *et al.*, 2017; Hakim, Shamardani
734 & Adesnik, 2018). Our results do not support an exclusive role for SST+ interneurons in slow
735 hippocampal gamma oscillations, but are consistent with an important role for SST+ interneurons
736 in gamma rhythmogenesis across cortical circuits. However, SST+ interneurons largely target the
737 dendritic domains of pyramidal cells, and thus it remains difficult to see how they could directly
738 contribute to the precise timing of pyramidal cell spiking during fast brain oscillations. SST+
739 bistratified interneurons have similar properties to fast spiking PV+ interneurons, and also form a
740 portion of synapses close to the soma (Somogyi & Klausberger, 2005; Muller & Remy, 2014), but
741 have been reported to exhibit decreased GABA release under cholinergic stimulation (Gulyás *et al.*,
742 2010). In our model, the dendritic location of SST+ is only represented by the slower time constant
743 of inhibition, but it highlights a potentially important role of hippocampal SST+ interneurons in
744 modulating the frequency of slow gamma oscillations that can be expressed in E-PV+ circuits.

745 While optogenetic manipulation of SST+ interneurons consistently disrupted slow gamma
746 oscillations, we found that photo-excitation of SST+ interneurons could also induce *de novo* fast
747 gamma oscillations. These GABAergic interneurons should provide a powerful source of circuit
748 inhibition (Somogyi & Klausberger, 2005; Pfeiffer *et al.*, 2013; Taniguchi *et al.*, 2011; Leão *et al.*, 2012;
749 Lovett-Barron *et al.*, 2012, 2014; Royer *et al.*, 2012; Urban-Ciecko & Barth, 2016), but we found that
750 sustained photo-excitation of SST+ interneurons did not significantly inhibit the activity of ChR2-
751 neurons, and that pulsed stimulation could drive network excitation. In our model, we could induce
752 fast gamma via photo-excitation of SST+ cells, but this was accompanied by a strong suppression of
753 activity in E and PV+ cells, and so it is likely that there are non-specific effects of ChR2 stimulation.
754 There have been reports of off-target expression in juvenile SST-Cre mice (Taniguchi *et al.*, 2011),
755 so there is still a possibility for pyramidal cell expression that we could not detect, or even SST+ cells
756 that co-release glutamate (Cattaneo *et al.*, 2019). An alternative possibility is that robust activation

757 of a dense plexus of SST+ axons in the dendritic layers is sufficient to induce spiking in pyramidal
758 neurons via ephaptic coupling (Anastassiou *et al.*, 2011; Ferenczi *et al.*, 2016) or changes in
759 extracellular ion concentration, which would be enhanced under interface recording conditions
760 (Octeau *et al.*, 2019), and counteract the effects of synaptic inhibition. The generation of fast gamma
761 oscillations appeared to depend on the maintenance of network excitability, as the oscillations were
762 attenuated by block of iGluRs. However, the spiking of the majority of SST- RS neurons was only
763 weakly coupled to the phase of light-induced fast gamma oscillations, and without a consistent
764 population spike phase preference, while light-sensitive putative SST+ interneurons showed reliable
765 phase-locking. This could be consistent with fast gamma oscillations representing rhythmic
766 dendritic inhibition from SST+ interneurons, with only weak effects on the spike rate and timing of
767 other neurons in the network.

768 The mechanism by which a network of SST+ interneurons might generate fast gamma oscillations
769 remains obscure. In neocortex, SST+ interneurons avoid inhibiting each other (Pfeffer *et al.*, 2013),
770 although there is evidence for sparse synaptic interactions between SST+ interneurons in the
771 hippocampus (Savanthrapadian *et al.*, 2014), and for more generic coupling via gap junctions (Baude
772 *et al.*, 2007). More experiments are required to resolve the mechanisms by which optogenetic
773 manipulation of interneurons influences hippocampal gamma oscillations, and whether SST+
774 neurons contribute to fast hippocampal gamma oscillations during theta and non-theta states *in*
775 *vivo* (Sullivan *et al.*, 2011). However, our findings suggest that SST+ interneurons exert powerful
776 control over the power and frequency of slow hippocampal gamma oscillations, and contribute to
777 the generation of fast gamma states.

778

779 **References**

- 780 Akam, T. & Kullmann, D.M. (2010) Oscillations and Filtering Networks Support Flexible Routing of
781 Information. *Neuron*. [Online] 67 (2), 308–320. Available from:
782 doi:10.1016/j.neuron.2010.06.019.
- 783 Akam, T., Oren, I., Mantoan, L., Ferenczi, E., et al. (2012) Oscillatory dynamics in the hippocampus
784 support dentate gyrus–CA3 coupling. *Nature Neuroscience*. [Online] 15 (5), 763–768.
785 Available from: doi:10.1038/nn.3081.
- 786 Anastassiou, C.A., Perin, R., Markram, H. & Koch, C. (2011) Ephaptic coupling of cortical neurons.
787 *Nature Neuroscience*. [Online] 14 (2), 217–223. Available from: doi:10.1038/nn.2727.
- 788 Andersen, P., Bliss, T.V.P. & Skrede, K.K. (1971) Unit analysis of hippocampal population spikes.
789 *Experimental Brain Research*. [Online] 13 (2), 208–221. Available from:
790 doi:10.1007/BF00234086.
- 791 Atallah, B. V. & Scanziani, M. (2009) Instantaneous Modulation of Gamma Oscillation Frequency by
792 Balancing Excitation with Inhibition. *Neuron*. [Online] 62 (4), 566–577. Available from:
793 doi:10.1016/J.NEURON.2009.04.027.
- 794 Bartos, M. & Elgueta, C. (2012) Functional characteristics of parvalbumin- and cholecystokinin-
795 expressing basket cells. *The Journal of Physiology*. [Online] 590 (4), 669–681. Available from:
796 doi:10.1113/jphysiol.2011.226175.
- 797 Bartos, M., Vida, I. & Jonas, P. (2007) Synaptic mechanisms of synchronized gamma oscillations in
798 inhibitory interneuron networks. *Nature reviews. Neuroscience*. [Online] 8 (1), 45–56.
799 Available from: doi:10.1038/nrn2044.
- 800 Basar-Eroglu, C., Brand, A., Hildebrandt, H., Karolina Kedzior, K., et al. (2007) Working memory
801 related gamma oscillations in schizophrenia patients. *International Journal of*

802 *Psychophysiology*. [Online] 64 (1), 39–45. Available from: doi:10.1016/j.ijpsycho.2006.07.007.

803 Bastos, A.M., Vezoli, J. & Fries, P. (2015) Communication through coherence with inter-areal
804 delays. *Current Opinion in Neurobiology*. [Online] 31, 173–180. Available from:
805 doi:10.1016/J.CONB.2014.11.001.

806 Baude, A., Bleasdale, C., Dalezios, Y., Somogyi, P., et al. (2007) Immunoreactivity for the GABAA
807 Receptor 1 Subunit, Somatostatin and Connexin36 Distinguishes Axoaxonic, Basket, and
808 Bistratified Interneurons of the Rat Hippocampus. *Cerebral Cortex*. [Online] 17 (9), 2094–
809 2107. Available from: doi:10.1093/cercor/bhl117.

810 Beierlein, M., Gibson, J.R. & Connors, B.W. (2000) A network of electrically coupled interneurons
811 drives synchronized inhibition in neocortex. *Nature Neuroscience*. [Online] 3 (9), 904–910.
812 Available from: doi:10.1038/78809.

813 Bettterton, R.T., Broad, L.M., Tsaneva-Atanasova, K. & Mellor, J.R. (2017) Acetylcholine modulates
814 gamma frequency oscillations in the hippocampus by activation of muscarinic M1 receptors
815 Panayiota Poirazi (ed.). *European Journal of Neuroscience*. [Online] 45 (12), 1570–1585.
816 Available from: doi:10.1111/ejn.13582.

817 Boyden, E.S., Zhang, F., Bamberg, E., Nagel, G., et al. (2005) Millisecond-timescale, genetically
818 targeted optical control of neural activity. *Nature Neuroscience*. [Online] 8 (9), 1263–1268.
819 Available from: doi:10.1038/nn1525.

820 Bragin, A., Jandó, G., Nádasdy, Z., Hetke, J., et al. (1995) Gamma (40-100 Hz) oscillation in the
821 hippocampus of the behaving rat. *The Journal of neuroscience : the official journal of the*
822 *Society for Neuroscience*. [Online] 15 (1 Pt 1), 47–60. Available from:
823 doi:https://doi.org/10.1523/JNEUROSCI.15-01-00047.1995.

824 Burns, S.P., Xing, D. & Shapley, R.M. (2011) Is gamma-band activity in the local field potential of V1

825 cortex a 'clock' or filtered noise? *The Journal of neuroscience : the official journal of the*
826 *Society for Neuroscience*. [Online] 31 (26), 9658–9664. Available from:
827 doi:10.1523/JNEUROSCI.0660-11.2011.

828 Butler, J.L., Hay, Y.A. & Paulsen, O. (2018) Comparison of three gamma oscillations in the mouse
829 entorhinal-hippocampal system. *European Journal of Neuroscience*. [Online] Available from:
830 doi:10.1111/ejn.13831.

831 Butler, J.L., Mendonça, P.R. F., Robinson, H.P.C. & Paulsen, O. (2016) Intrinsic Cornu Ammonis
832 Area 1 Theta-Nested Gamma Oscillations Induced by Optogenetic Theta Frequency
833 Stimulation. *The Journal of neuroscience : the official journal of the Society for Neuroscience*.
834 [Online] 36 (15), 4155–4169. Available from: doi:10.1523/JNEUROSCI.3150-15.2016.

835 Butler, J.L. & Paulsen, O. (2014) The Hippocampal Cacophony: Multiple Layers of Communication.
836 *Neuron*. [Online] 84 (2), 251–253. Available from: doi:10.1016/J.NEURON.2014.10.017.

837 Buzsáki, G. (2002) Theta Oscillations in the Hippocampus. *Neuron*. [Online] 33 (3), 325–340.
838 Available from: doi:10.1016/S0896-6273(02)00586-X.

839 Buzsáki, G. & Wang, X.-J. (2012) Mechanisms of Gamma Oscillations. *Annual Review of*
840 *Neuroscience*. [Online] 35 (1), 203–225. Available from: doi:10.1146/annurev-neuro-062111-
841 150444.

842 Cardin, J.A. (2016) Snapshots of the Brain in Action: Local Circuit Operations through the Lens of γ
843 Oscillations. *Journal of Neuroscience*. [Online] 36 (41), 10496–10504. Available from:
844 doi:10.1523/JNEUROSCI.1021-16.2016.

845 Cardin, J.A., Carlén, M., Meletis, K., Knoblich, U., et al. (2009) Driving fast-spiking cells induces
846 gamma rhythm and controls sensory responses. *Nature*. [Online] 459 (7247), 663–667.
847 Available from: doi:10.1038/nature08002.

848 Cattaneo, S., Zaghi, M., Maddalena, R., Bedogni, F., et al. (2019) Somatostatin-Expressing
849 Interneurons Co-Release GABA and Glutamate onto Different Postsynaptic Targets in the
850 Striatum. *bioRxiv*. [Online] 566984. Available from: doi:10.1101/566984.

851 Chen, G., Zhang, Y., Li, X., Zhao, X., et al. (2017) Distinct Inhibitory Circuits Orchestrate Cortical
852 beta and gamma Band Oscillations. *Neuron*. [Online] 96 (6), 1403-1418.e6. Available from:
853 doi:10.1016/j.neuron.2017.11.033.

854 Chow, B.Y., Han, X., Dobry, A.S., Qian, X., et al. (2010) High-performance genetically targetable
855 optical neural silencing by light-driven proton pumps. *Nature*. [Online] 463 (7277), 98–102.
856 Available from: doi:10.1038/nature08652.

857 Colgin, L.L., Denninger, T., Fyhn, M., Hafting, T., et al. (2009) Frequency of gamma oscillations
858 routes flow of information in the hippocampus. *Nature*. [Online] 462 (7271), 353–357.
859 Available from: doi:10.1038/nature08573.

860 Craig, M.T. & McBain, C.J. (2015) Fast gamma oscillations are generated intrinsically in CA1
861 without the involvement of fast-spiking basket cells. *The Journal of neuroscience : the official*
862 *journal of the Society for Neuroscience*. [Online] 35 (8), 3616–3624. Available from:
863 doi:10.1523/JNEUROSCI.4166-14.2015.

864 Csicsvari, J., Jamieson, B., Wise, K.D. & Buzsáki, G. (2003) Mechanisms of gamma oscillations in the
865 hippocampus of the behaving rat. *Neuron*. [Online] 37 (2), 311–322. Available from:
866 doi:10.1016/S0896-6273(02)01169-8.

867 Devalle, F., Roxin, A. & Montbrió, E. (2017) Firing rate equations require a spike synchrony
868 mechanism to correctly describe fast oscillations in inhibitory networks. *PLoS Computational*
869 *Biology*. [Online] 13 (12), e1005881. Available from: doi:10.1371/journal.pcbi.1005881.

870 El-Gaby, M., Zhang, Y., Wolf, K., Schwiening, C.J., et al. (2016) Archaelhodopsin Selectively and

871 Reversibly Silences Synaptic Transmission through Altered pH. *Cell Reports*. [Online] 16 (8),
872 2259–2268. Available from: doi:10.1016/J.CELREP.2016.07.057.

873 Fee, M.S., Mitra, P.P. & Kleinfeld, D. (1996) Automatic sorting of multiple unit neuronal signals in
874 the presence of anisotropic and non-Gaussian variability. *Journal of Neuroscience Methods*.
875 [Online] 69 (2), 175–188. Available from: doi:10.1016/S0165-0270(96)00050-7.

876 Ferenczi, E.A., Vierock, J., Atsuta-Tsunoda, K., Tsunoda, S.P., et al. (2016) Optogenetic approaches
877 addressing extracellular modulation of neural excitability. *Scientific Reports*. [Online] 6 (1),
878 23947. Available from: doi:10.1038/srep23947.

879 Fisahn, A., Pike, F.G., Buhl, E. H. & Paulsen, O. (1998) Cholinergic induction of network oscillations
880 at 40 Hz in the hippocampus in vitro. *Nature*. [Online] 394 (6689), 186–189. Available from:
881 doi:10.1038/28179.

882 Fries, P. (2005) A mechanism for cognitive dynamics: neuronal communication through neuronal
883 coherence. *Trends in Cognitive Sciences*. [Online] 9 (10), 474–480. Available from:
884 doi:10.1016/J.TICS.2005.08.011.

885 Fries, P. (2015) Rhythms for Cognition: Communication through Coherence. *Neuron*. [Online] 88
886 (1), 220–235. Available from: doi:10.1016/j.neuron.2015.09.034.

887 Fries, P., Reynolds, J.H., Rorie, A.E. & Desimone, R. (2001) Modulation of oscillatory neuronal
888 synchronization by selective visual attention. *Science (New York, N.Y.)*. [Online] 291 (5508),
889 1560–1563. Available from: doi:10.1126/science.291.5508.1560.

890 Fuchs, E.C., Zivkovic, A.R., Cunningham, M.O., Middleton, S., et al. (2007) Recruitment of
891 Parvalbumin-Positive Interneurons Determines Hippocampal Function and Associated
892 Behavior. *Neuron*. [Online] 53 (4), 591–604. Available from:
893 doi:10.1016/J.NEURON.2007.01.031.

894 Gloveli, T., Dugladze, T., Saha, S., Monyer, H., et al. (2005) Differential involvement of
 895 oriens/pyramidal interneurons in hippocampal network oscillations In vitro. *The Journal of*
 896 *Physiology*. [Online] 562 (1), 131–147. Available from: doi:10.1113/jphysiol.2004.073007.

897 Gulyás, A.I., Szabó, G.G., Ulbert, I., Holderith, N., et al. (2010) Parvalbumin-containing fast-spiking
 898 basket cells generate the field potential oscillations induced by cholinergic receptor activation
 899 in the hippocampus. *The Journal of neuroscience : the official journal of the Society for*
 900 *Neuroscience*. [Online] 30 (45), 15134–15145. Available from: doi:10.1523/JNEUROSCI.4104-
 901 10.2010.

902 Hájos, N., Pálhalini, J., Mann, E.O., Németh, B., et al. (2004) Spike timing of distinct types of
 903 GABAergic interneuron during hippocampal gamma oscillations in vitro. *Journal of*
 904 *Neuroscience*. [Online] 24 (41), 9127–9137. Available from: doi:10.1523/JNEUROSCI.2113-
 905 04.2004.

906 Hájos, N. & Paulsen, O. (2009) Network mechanisms of gamma oscillations in the CA3 region of the
 907 hippocampus. *Neural Networks*. [Online] 22 (8), 1113–1119. Available from:
 908 doi:10.1016/j.neunet.2009.07.024.

909 Hakim, R., Shamardani, K. & Adesnik, H. (2018) A neural circuit for gamma-band coherence across
 910 the retinotopic map in mouse visual cortex. *eLife*. [Online] 7, e28569. Available from:
 911 doi:10.7554/eLife.28569.

912 Hasenstaub, A., Shu, Y., Haider, B., Kraushaar, U., et al. (2005) Inhibitory Postsynaptic Potentials
 913 Carry Synchronized Frequency Information in Active Cortical Networks. *Neuron*. [Online] 47
 914 (3), 423–435. Available from: doi:10.1016/J.NEURON.2005.06.016.

915 Herman, A.M., Huang, L., Murphey, D.K., Garcia, I., et al. (2014) Cell type-specific and time-
 916 dependent light exposure contribute to silencing in neurons expressing Channelrhodopsin-2.

917 *eLife*. [Online] 3, e01481. Available from: doi:10.7554/eLife.01481.

918 Herrmann, C.S. & Demiralp, T. (2005) Human EEG gamma oscillations in neuropsychiatric
 919 disorders. *Clinical Neurophysiology*. [Online] 116 (12), 2719–2733. Available from:
 920 doi:10.1016/J.CLINPH.2005.07.007.

921 Hofer, S.B., Ko, H., Pichler, B., Vogelstein, J., et al. (2011) Differential connectivity and response
 922 dynamics of excitatory and inhibitory neurons in visual cortex. *Nature Neuroscience*. [Online]
 923 14 (8), 1045–1052. Available from: doi:10.1038/nn.2876.

924 Hu, H., Gan, J. & Jonas, P. (2014) Interneurons. Fast-spiking, parvalbumin+ GABAergic
 925 interneurons: from cellular design to microcircuit function. *Science (New York, N.Y.)*. [Online]
 926 345 (6196), 1255263. Available from: doi:10.1126/science.1255263.

927 Huang, S., & Uusisaari, M. Y. (2013). Physiological temperature during brain slicing enhances the
 928 quality of acute slice preparations. *Frontiers in Cellular Neuroscience*, 7, 48.
 929 <https://doi.org/10.3389/fncel.2013.00048>

930 Kim, D., Jeong, H., Lee, J., Ghim, J.-W., et al. (2016) Distinct Roles of Parvalbumin- and
 931 Somatostatin-Expressing Interneurons in Working Memory. *Neuron*. [Online] 92 (4), 902–915.
 932 Available from: doi:10.1016/J.NEURON.2016.09.023.

933 Kohus, Z., Káli, S., Rovira-Esteban, L., Schlingloff, D., et al. (2016) Properties and dynamics of
 934 inhibitory synaptic communication within the CA3 microcircuits of pyramidal cells and
 935 interneurons expressing parvalbumin or cholecystokinin. *The Journal of Physiology*. [Online]
 936 594 (13), 3745–3774. Available from: doi:10.1113/JP272231.

937 Lasztóczy, B. & Klausberger, T. (2016) Hippocampal Place Cells Couple to Three Different Gamma
 938 Oscillations during Place Field Traversal. *Neuron*. [Online] 91 (1), 34–40. Available from:
 939 doi:10.1016/J.NEURON.2016.05.036.

- 940 Leão, R.N., Mikulovic, S., Leão, K.E., Munguba, H., et al. (2012) OLM interneurons differentially
 941 modulate CA3 and entorhinal inputs to hippocampal CA1 neurons. *Nature Neuroscience*.
 942 [Online] 15 (11), 1524–1530. Available from: doi:10.1038/nn.3235.
- 943 Lovett-Barron, M., Kaifosh, P., Kheirbek, M.A., Danielson, N., et al. (2014) Dendritic inhibition in
 944 the hippocampus supports fear learning. *Science (New York, N.Y.)*. [Online] 343 (6173), 857–
 945 863. Available from: doi:10.1126/science.1247485.
- 946 Lovett-Barron, M., Turi, G.F., Kaifosh, P., Lee, P.H., et al. (2012) Regulation of neuronal input
 947 transformations by tunable dendritic inhibition. *Nature Neuroscience*. [Online] 15 (3), 423–
 948 430. Available from: doi:10.1038/nn.3024.
- 949 Ma, Y., Hu, H., Berrebi, A.S., Mathers, P.H., et al. (2006) Distinct subtypes of somatostatin-
 950 containing neocortical interneurons revealed in transgenic mice. *The Journal of neuroscience :*
 951 *the official journal of the Society for Neuroscience*. [Online] 26 (19), 5069–5082. Available
 952 from: doi:10.1523/JNEUROSCI.0661-06.2006.
- 953 Mann, E.O., Radcliffe, C.A. & Paulsen, O. (2005) Hippocampal gamma-frequency oscillations: from
 954 interneurons to pyramidal cells, and back. *The Journal of Physiology*. [Online] 562 (1), 55–63.
 955 Available from: doi:10.1113/jphysiol.2004.078758.
- 956 Mann, E.O., Suckling, J.M., Hajos, N., Greenfield, S.A., et al. (2005) Perisomatic Feedback Inhibition
 957 Underlies Cholinergically Induced Fast Network Oscillations in the Rat Hippocampus In Vitro.
 958 *Neuron*. [Online] 45 (1), 105–117. Available from: doi:10.1016/j.neuron.2004.12.016.
- 959 Muller, C. & Remy, S. (2014) Dendritic inhibition mediated by O-LM and bistratified interneurons
 960 in the hippocampus. *Frontiers in Synaptic Neuroscience*. [Online] 6, 23. Available from:
 961 doi:10.3389/fnsyn.2014.00023.
- 962 Nagel, G., Szellas, T., Huhn, W., Kateriya, S., et al. (2003) Channelrhodopsin-2, a directly light-gated

963 cation-selective membrane channel. *Proceedings of the National Academy of Sciences of the*
964 *United States of America*. [Online] 100 (24), 13940–13945. Available from:
965 doi:10.1073/pnas.1936192100.

966 Oceau, J.C., Gangwani, M.R., Allam, S.L., Tran, D., et al. (2019) Transient, Consequential Increases
967 in Extracellular Potassium Ions Accompany Channelrhodopsin2 Excitation. *Cell Reports*.
968 [Online] 27 (8), 2249–2261.e7. Available from: doi:10.1016/j.celrep.2019.04.078.

969 Oren, I., Hájos, N. & Paulsen, O. (2010) Identification of the current generator underlying
970 cholinergically induced gamma frequency field potential oscillations in the hippocampal CA3
971 region. *The Journal of Physiology*. [Online] 588 (5), 785–797. Available from:
972 doi:10.1113/jphysiol.2009.180851.

973 Oren, I., Mann, E.O., Paulsen, O. & Hájos, N. (2006) Synaptic currents in anatomically identified
974 CA3 neurons during hippocampal gamma oscillations in vitro. *The Journal of neuroscience :*
975 *the official journal of the Society for Neuroscience*. [Online] 26 (39), 9923–9934. Available
976 from: doi:10.1523/JNEUROSCI.1580-06.2006.

977 Packer, A.M. & Yuste, R. (2011) Dense, unspecific connectivity of neocortical parvalbumin-positive
978 interneurons: a canonical microcircuit for inhibition? *The Journal of neuroscience : the official*
979 *journal of the Society for Neuroscience*. [Online] 31 (37), 13260–13271. Available from:
980 doi:10.1523/JNEUROSCI.3131-11.2011.

981 Penttonen, M., Kamondi, A., Acsady, L. & Buzsaki, G. (1998) Gamma frequency oscillation in the
982 hippocampus of the rat: intracellular analysis in vivo. *European Journal of Neuroscience*.
983 [Online] 10 (2), 718–728. Available from: doi:10.1046/j.1460-9568.1998.00096.x.

984 Pfeffer, C.K., Xue, M., He, M., Huang, Z.J., et al. (2013) Inhibition of inhibition in visual cortex: the
985 logic of connections between molecularly distinct interneurons. *Nature Neuroscience*.

986 [Online] 16 (8), 1068–1076. Available from: doi:10.1038/nn.3446.

987 Pike, F.G., Goddard, R.S., Suckling, J.M., Ganter, P., et al. (2000) Distinct frequency preferences of
 988 different types of rat hippocampal neurones in response to oscillatory input currents. *The*
 989 *Journal of Physiology*. [Online] 529 (1), 205–213. Available from: doi:10.1111/j.1469-
 990 7793.2000.00205.x.

991 Pouille, F. & Scanziani, M. (2001) Enforcement of temporal fidelity in pyramidal cells by somatic
 992 feed-forward inhibition. *Science (New York, N.Y.)*. [Online] 293 (5532), 1159–1163. Available
 993 from: doi:10.1126/science.1060342.

994 Quian Quiroga, R. (2009) What is the real shape of extracellular spikes? *Journal of Neuroscience*
 995 *Methods*. [Online] 177 (1), 194–198. Available from: doi:10.1016/J.JNEUMETH.2008.09.033.

996 Quiroga, R.Q., Nadasdy, Z. & Ben-Shaul, Y. (2004) Unsupervised Spike Detection and Sorting with
 997 Wavelets and Superparamagnetic Clustering. *Neural Computation*. [Online] 16 (8), 1661–
 998 1687. Available from: doi:10.1162/089976604774201631.

999 Ray, S. & Maunsell, J.H.R. (2015) Do gamma oscillations play a role in cerebral cortex? *Trends in*
 1000 *Cognitive Sciences*. [Online] 19 (2), 78–85. Available from: doi:10.1016/J.TICS.2014.12.002.

1001 Royer, S. eacute bastien, Zemelman, B. V, Losonczy, A., Kim, J., et al. (2012) Control of timing, rate
 1002 and bursts of hippocampal place cells by dendritic and somatic inhibition. *Nature*
 1003 *Neuroscience*. [Online] 15 (5), 1–10. Available from: doi:10.1038/nn.3077.

1004 Savanthrapadian, S., Meyer, T., Elgueta, C., Booker, S.A., et al. (2014) Synaptic Properties of SOM-
 1005 and CCK-Expressing Cells in Dentate Gyrus Interneuron Networks. *Journal of Neuroscience*.
 1006 [Online] 34 (24), 8197–8209. Available from: doi:10.1523/JNEUROSCI.5433-13.2014.

1007 Schomburg, E.W., Fernández-Ruiz, A., Mizuseki, K., Berényi, A., et al. (2014) Theta phase
 1008 segregation of input-specific gamma patterns in entorhinal-hippocampal networks. *Neuron*.

1009 [Online] 84 (2), 470–485. Available from: doi:10.1016/j.neuron.2014.08.051.

1010 Sohal, V.S. (2016) How Close Are We to Understanding What (if Anything) Oscillations Do in
 1011 Cortical Circuits? *Journal of Neuroscience*. [Online] 36 (41), 10489–10495. Available from:
 1012 doi:10.1523/JNEUROSCI.0990-16.2016.

1013 Sohal, V.S., Zhang, F., Yizhar, O. & Deisseroth, K. (2009) Parvalbumin neurons and gamma rhythms
 1014 enhance cortical circuit performance. *Nature*. [Online] 459 (7247), 698–702. Available from:
 1015 doi:10.1038/nature07991.

1016 Somogyi, P. & Klausberger, T. (2005) Defined types of cortical interneurone structure space and
 1017 spike timing in the hippocampus. *The Journal of physiology*. [Online] 562 (Pt 1), 9–26.
 1018 Available from: doi:10.1113/jphysiol.2004.078915.

1019 Spellman, T., Rigotti, M., Ahmari, S.E., Fusi, S., et al. (2015) Hippocampal–prefrontal input supports
 1020 spatial encoding in working memory. *Nature*. [Online] 522 (7556), 309–314. Available from:
 1021 doi:10.1038/nature14445.

1022 Sullivan, D., Csicsvari, J., Mizuseki, K., Montgomery, S., et al. (2011) Relationships between
 1023 hippocampal sharp waves, ripples, and fast gamma oscillation: influence of dentate and
 1024 entorhinal cortical activity. *The Journal of neuroscience : the official journal of the Society for*
 1025 *Neuroscience*. [Online] 31 (23), 8605–8616. Available from: doi:10.1523/JNEUROSCI.0294-
 1026 11.2011.

1027 Taniguchi, H., He, M., Wu, P., Kim, S., et al. (2011) A Resource of Cre Driver Lines for Genetic
 1028 Targeting of GABAergic Neurons in Cerebral Cortex. *Neuron*. [Online] 71 (6), 995–1013.
 1029 Available from: doi:10.1016/J.NEURON.2011.07.026.

1030 Tukker, J.J., Fuentealba, P., Hartwich, K., Somogyi, P., et al. (2007) *Cell Type-Specific Tuning of*
 1031 *Hippocampal Interneuron Firing during Gamma Oscillations*. [Online] 27 (31), 8184–8189.

- 1032 Available from: doi:10.1523/JNEUROSCI.1685-07.2007.
- 1033 Tukker, J.J., Lasztóczy, B., Katona, L., Roberts, J.D.B., et al. (2013) Distinct dendritic arborization and
 1034 in vivo firing patterns of parvalbumin-expressing basket cells in the hippocampal area CA3.
 1035 *The Journal of neuroscience : the official journal of the Society for Neuroscience*. [Online] 33
 1036 (16), 6809–6825. Available from: doi:10.1523/JNEUROSCI.5052-12.2013.
- 1037 Uhlhaas, P.J. & Singer, W. (2010) Abnormal neural oscillations and synchrony in schizophrenia.
 1038 *Nature Reviews Neuroscience*. [Online] 11 (2), 100–113. Available from: doi:10.1038/nrn2774.
- 1039 Uhlhaas, P.J. & Singer, W. (2006) Neural Synchrony in Brain Disorders: Relevance for Cognitive
 1040 Dysfunctions and Pathophysiology. *Neuron*. [Online] 52 (1), 155–168. Available from:
 1041 doi:10.1016/j.neuron.2006.09.020.
- 1042 Urban-Ciecko, J. & Barth, A.L. (2016) Somatostatin-expressing neurons in cortical networks. *Nature*
 1043 *Reviews Neuroscience*. [Online] 17 (7), 401–409. Available from: doi:10.1038/nrn.2016.53.
- 1044 Veit, J., Hakim, R., Jadi, M.P., Sejnowski, T.J., et al. (2017) Cortical gamma band synchronization
 1045 through somatostatin interneurons. *Nature Neuroscience*. [Online] 20 (7), 951–959. Available
 1046 from: doi:10.1038/nn.4562.
- 1047 Whittington, M.A., Traub, R.D. & Jefferys, J.G.R. (1995) Synchronized oscillations in interneuron
 1048 networks driven by metabotropic glutamate receptor activation. *Nature*. [Online] 373 (6515),
 1049 612–615. Available from: doi:10.1038/373612a0.
- 1050 Wierenga, C.. & Wadman, W.. (2003) Functional relation between interneuron input and
 1051 population activity in the rat hippocampal cornu ammonis 1 area. *Neuroscience*. [Online] 118
 1052 (4), 1129–1139. Available from: doi:10.1016/S0306-4522(03)00060-5.
- 1053 Womelsdorf, T. & Everling, S. (2015) Long-Range Attention Networks: Circuit Motifs Underlying
 1054 Endogenously Controlled Stimulus Selection. *Trends in Neurosciences*. [Online] 38 (11), 682–

1055 700. Available from: doi:10.1016/J.TINS.2015.08.009.

1056 Yamamoto, J., Suh, J., Takeuchi, D. & Tonegawa, S. (2014) Successful Execution of Working
1057 Memory Linked to Synchronized High-Frequency Gamma Oscillations. *Cell*. [Online] 157 (4),
1058 845–857. Available from: doi:10.1016/J.CELL.2014.04.009.

1059 Zar, J.H. (1999) Biostatistical analysis. In: *Prentice Hall*. 4th edition. Englewood Cliffs, New Jersey.
1060 p. 929.

1061

1062

1063

Figure legends

1064

Figure 1: Sustained photo-inhibition of PV+ interneurons suppresses the power of gamma

1065

oscillations. A, Confocal image of ventral hippocampus slice from a PV-cre mouse injected

1066

intrahippocampally with AAV-Arch3 eYFP. CA3 = Cornu Ammonis 3, DG = Dentate Gyrus, Pyr. =

1067

stratum pyramidale, Rad. = stratum radiatum, Or. = stratum oriens. Scale bar = 200 μ m. **B**, Current

1068

clamp recording of an ArchT-GFP expressing PV+ cell from CA3 area, showing responses to

1069

depolarising and hyperpolarising current steps, and fast-spiking phenotype. **C**, Potent

1070

hyperpolarisation of four PV+ interneurons during green light illumination in aCSF (1.45 mW). **D**,

1071

Illustration of the electrophysiological setup, with coloured line indicating the region of CA3

1072

stratum pyramidale from which recordings were obtained. **E**, Cholinergically-induced oscillations

1073

(5 μ M Cch) were suppressed during PV+ interneuron photo-inhibition (LED, 530 nm, approx. 4.25

1074

mW). **F**, Representative power spectra before (black) and during (green) LED illumination (arrows

1075

indicate peaks in the power spectra). **G**, Power area in the 20-100 Hz band normalised to baseline

1076

(Pre (Off)) during (On) and after LED stimulation (Off (Post)) (n = 35). **H**, Peak frequency for

1077

experiments when the oscillation was not abolished (n = 31/35). **I**, Change in power area plotted

1078

against change in peak frequency. **J**, Stronger photo-inhibition was achieved using high power

1079

laser illumination (approx. 18.6 mW). Top: Change in power area normalised to baseline and,

1080

Bottom: Peak frequency of the oscillation calculated in 1 second bins across experiments (n = 14).

1081

K, Mean change in power area normalised to baseline (n = 14). **L**, Mean peak frequency for trials

1082

when the oscillation was not abolished (n = 13). *p < 0.05, ***p < 0.001, n.s. p \geq 0.05. Changes in

1083

peak frequency were analysed using rmANOVA, followed by post-hoc paired t-tests with

1084

correction for multiple comparisons. Solid brackets represent paired t-tests and standalone star

1085

symbols represent one-sample t-test versus normalised baseline. Grey lines represent single

1086

experiments.

1087

1088 **Figure 2: Sustained photo-inhibition of SST+ interneurons suppresses gamma power and**
1089 **increases frequency. A**, Confocal image of ventral hippocampus slice from SST-cre mice with eYFP-
1090 Arch3 expression. Scale bar = 200 μ m. **B**, Quantification of fluorescence expression profile in PV (n
1091 = 18) and SST (n = 21) ArchT-GFP expressing slices. **C**, Current clamp recording of an SST+ cell from
1092 CA3 area, showing responses to depolarising and hyperpolarising current steps. **D**, Potent
1093 hyperpolarisation of four SST+ interneurons during green light illumination (1.45 mW). **E**,
1094 Representative LFP recordings illustrating effect of SST+ interneuron photo-inhibition (LED, 530
1095 nm, approx. 4.25 mW). **F**, Representative power spectra before (black) and during (green) LED
1096 illumination (arrows indicate peaks in the power spectra). **G**, Power area in the 20-100 Hz band
1097 normalised to baseline (Pre (Off)) during (On) and after LED stimulation (Post (Off)) (n = 44). **H**,
1098 Peak frequency for experiments when the oscillation was not abolished (n = 33/44). **I**, Change in
1099 power area plotted against change in peak frequency. **J**, Effects of sustained laser illumination
1100 (approx. 18.6 mW) on normalised power area (top) and peak frequency (bottom) calculated in 1
1101 second bins (n = 17). **K**, Mean normalised power area (n = 17). **L**, Mean peak frequency for trials
1102 when the oscillation was not abolished (n = 11/17). *p < 0.05, **p < 0.01, ***p < 0.001, n.s. p >= 0.05. Solid brackets represent paired t-tests and standalone star symbols represent one-sample t-
1103 test versus normalised baseline. Grey lines represent single experiments.

1105

1106 **Figure 3: Rhythmic photo-excitation of either PV+ or SST+ interneurons entrains Cch-induced**
1107 **gamma oscillations. A-B**, Confocal images of ventral hippocampus (350 μ m slice) from PV-cre (A)
1108 and SST-cre (B) mice with mCherry-ChR2 expression. Scale bar = 200 μ m. **C-D**, Spiking responses of
1109 PV+ and SST+ interneurons during 40 Hz light pulses (1-5 ms pulse width), characterised in terms
1110 of spike rate (C) and spike fidelity (D). **E-F**, Entrainment of Cch-induced oscillations to 40 Hz light

1111 pulses in PV-cre (*E*) and SST-cre (*F*) mice expressing mCherry-ChR2 (1 ms pulse width; blue light
 1112 illumination at 5.5 mW), shown in LFP traces (top) and normalised wavelet spectrum (bottom).
 1113 Brighter colours represent larger magnitudes. **G-H**, Normalised average waveform following two
 1114 consecutive 1 ms pulses at 40 Hz from each experiment (PV+: n = 15/18; SST+: n = 19/22). Bold line
 1115 is the population average, thinner lines represent individual experiments and shaded area is the
 1116 SEM. Arrows indicate initial negative peak. **I-K**, Peak frequency of oscillation before (Pre (Off)),
 1117 during (On) and after (Post (Off)) light stimulation, for PV+ with 1 ms pulse width (*I*; n = 18/18),
 1118 PV+ with 5 ms pulse width (*J*; n = 13/13; several overlapping traces) and SST+ with 1 ms pulse
 1119 width (*K*; n = 19/22). Note that experiments entrained at 20 Hz reflect suppression of alternate
 1120 gamma cycles.

1121

1122 **Figure 4: Network excitation arising from photo-excitation in SST-cre mice.** **A**, LFP responses to
 1123 40 Hz stimulation in slices from SST-ChR2 mice recorded in aCSF (1 ms pulse width; 5.5 mW). **B**,
 1124 Average waveform before (black) and after application of 20 μ M CNQX and 40 μ M AP5 (orange). **C**,
 1125 Effect of ionotropic glutamate receptor (iGluR) blockers on the amplitude of negative ($t = -0.61$, p
 1126 $= 0.58$) and positive peaks ($t = 3.49$, $p = 0.03$, $n = 4$; paired t-test). iGluR blockers used: 20 μ M
 1127 CNQX, 40 μ M AP5, $n = 3$; 20 μ M CNQX, $n = 1$. **D**, Average waveform before (black) and after
 1128 application of 10 μ M gabazine (GBZ; orange). **E**, Effect of GBZ on absolute amplitude ($n = 3$). **F**,
 1129 Photo-excitation of SST+ interneurons induces epileptiform bursts during following GABA_AR
 1130 blockage ($n = 2$ at 20 μ M bicuculine (BIC), $n = 2$ at 10 μ M GBZ). **G**, (i) Voltage-clamp recording from
 1131 putative pyramidal cell during photo-activation of SST+ interneurons (1.53 mW), and held at 0 mV
 1132 (top) and -70mV (bottom) to isolate IPSCs and EPSCs, respectively. (ii) Across all cells, the mean
 1133 EPSCs (blue) were smaller than IPSCs (orange) during SST+ interneuron photo-activation ($n = 18$).
 1134 **H-I**, Perforated patch current-clamp recordings from putative CA3 pyramidal cell in SST-cre mice

1135 expressing ChR2-mcherry, showing responses to depolarising and hyperpolarising current steps
1136 (*H*), and hyperpolarisation in response to light stimulation (1.53 mW; *n* = 6). Grey traces represent
1137 individual cells, black trace the average and dark grey shaded area the SEM.

1138

1139 **Figure 5: Sustained photo-excitation of PV+ interneurons decreases the power and increases the**
1140 **frequency of Cch-induced gamma oscillations. A-B**, Representative LFP recordings from CA3 area
1141 illustrating effect of PV+ interneurons photo-excitation (155 μ W) on gamma oscillations (*A*), along
1142 with its respective power spectrum (*B*; arrows indicate power spectrum peaks). **C-D**, Time course
1143 of normalised power area (*C*) and peak frequency (*D*), each calculated in 0.5 second bins across
1144 experiments (*n* = 12). **E**, Mean changes in normalised power area. **F**, Mean peak frequency;
1145 rmANOVA: $F(1.14, 12.50) = 44.14$, $p < 0.001$. **G-H**, Normalised power area (*G*) and changes in peak
1146 frequency (*H*) plotted against light intensity (*n* = 12). **I**, Strong and sustained blue light illumination
1147 (5.5 mW) induces a collapse of Cch-induced oscillations, as seen in LFP traces (top) and normalised
1148 wavelet spectrum (bottom). **J**, Effect of strong illumination on mean normalised power area (*n*
1149 total = 23; *n* = 14 at 5.5 mW and *n* = 9 at 2.2 mW). **K-L**, Strong and sustained blue light illumination
1150 does not induced increases in network activity in aCSF. *** $p < 0.001$, n.s. $p \geq 0.05$. Solid brackets
1151 represent paired t-tests and standalone star symbols represent one-sample t-test versus
1152 normalised baseline. Grey lines represent single experiments.

1153

1154 **Figure 6: Multi-unit recordings during PV+ interneuron sustained photo-excitation in**
1155 **hippocampal slices with Cch-induced gamma oscillations. A**, Schematic diagram of the
1156 hippocampus illustrating MEA recordings during blue light illumination (5.5 mW) in CA3. **B**,
1157 Representative average spike waveforms of PV+ (single unit ; green) and RS (multi-unit; black)
1158 neurons. **C**, Spike time histograms of the representative neurons during sustained light

illumination. **D-E**, Mean spike time histograms during step illumination (*D*) and sinusoidal theta stimulation (8 Hz; *E*), calculated from the fraction of total spike counts in each bin for each clustered neuron. **F**, Spike phase histograms relative to ongoing gamma-frequency oscillations, calculated from the fraction of total spike counts. **G**, Sustained activation index (top), modulation index (middle) and vector length (bottom). **H**, Instantaneous amplitude of the Hilbert transform during theta photo-activation (1 mW) overlaid across experiments (grey traces, *n* = 12), black represents the mean and dark grey the SEM. Dotted lines highlight peaks and troughs in the light waveform. **I**, Intracellular current-clamp recordings from pyramidal cells in aCSF, showing responses to current steps (left) and hyperpolarisation in response to PV+ interneuron photo-activation (right; *n* = 4).

1169

Figure 7: Sustained photo-excitation of SST+ interneurons decreases the power and increases the frequency of Cch-induced gamma oscillations, but can also induce high-frequency oscillations. A-B, Representative LFP recordings from CA3 area illustrating effect of SST+ interneurons photo-excitation (155 μ W) on gamma oscillations (*A*), along with the respective power spectra (*B*; arrows indicate peaks in the power spectra). **C-D** Time course of normalised power area (*C*) and peak frequency (*D*), each calculated in 0.5 second bins across experiments (*n* = 12). **E**, Mean changes in normalised power area. **F**, Changes in mean peak frequency; rmANOVA: $F(1.05, 11.59) = 15.05$, $p = 0.002$. **G-H**, Normalised power area (*G*) and changes in peak frequency (*H*) plotted against light intensity (*n* = 12). **I**, Strong and sustained blue light illumination (5.5 mW), that does not cause the collapse of Cch-induced oscillations, induces high-frequency oscillations, as seen in LFP traces (top) and normalised wavelet spectrum (bottom). **J**, Normalised power during SST+ interneurons cell photo-activation (*n* = 31). **K**, Peak frequency of oscillations that were not abolished during strong light illumination (*n* remaining = 16/31: *n* = 4 at 5.5 mW and *n* = 12 at 2.2

1183 mW); rmANOVA: $F(1.03, 15.39) = 31.45$, $p < 0.001$. Changes in peak frequency were analysed
 1184 using rmANOVA, followed by post-hoc paired t-tests with correction for multiple comparisons. **L**,
 1185 Responses to laser illumination (approx. 18.6 mW) in SST-cre mice expressing ArchT-GFP with and
 1186 without the presence of Cch. Orange squares represent the bottom sections of LFP that were
 1187 magnified. **M**, Changes in normalised power area calculated in 1 second bins across experiments
 1188 ($n = 3$) in aCSF only. Dotted lines indicate the duration of laser illumination. * $p < 0.05$, ** $p < 0.01$,
 1189 *** $p < 0.001$, n.s. $p \geq 0.05$. Solid brackets represent paired t-tests and standalone star symbols
 1190 represent one-sample t-test versus normalised baseline. Grey lines represent single experiments.

1191

1192 **Figure 8: Photo-activation of SST+ interneurons induces *de novo* oscillations in the absence of**
 1193 **Cch. A-B**, Representative LFP recordings from CA3 illustrating induction of high-frequency
 1194 oscillations by step (A) and theta-modulated (B) blue light illumination (10 mW), as seen in LFP
 1195 traces (top) and normalised wavelet spectrum (bottom). **C**, Change in log power compared to
 1196 baseline during step ($n = 16$) and theta-modulated blue light illumination ($n = 17$). **D**, Peak
 1197 frequency of the *de novo* oscillations is higher when induced by theta when compared to tonic
 1198 stimulation; two-sample t-test, *** $p < 0.001$. **E-F**, Power area (E) and peak frequency (F) plotted
 1199 against light intensity of theta photo-activation ($n = 12$). The black line is the mean response and
 1200 the dark-grey shaded area represents SEM. **G-H**, pharmacology of de-novo oscillations induced by
 1201 sinusoidal blue light illumination in SST-cre mice expressing ChR2-mcherry (1 - 10 mW).
 1202 Representative LFP recording in CA3 before (top) and after (bottom) application of G.i) iGluR
 1203 blockers and H.i) GABA_AR blockers. Power-area change before (control) and after application of
 1204 G.ii) iGluR blockers and H.ii) GABA_AR blockers. iGluR blockers used: 20 μ M CNQX, 40 μ M AP5, $n =$
 1205 3; 10 μ M CNQX, 20 μ M AP5, $n = 1$; 20 μ M CNQX, $n = 1$; 3mM kynurenic acid, $n = 3$. GABA_AR
 1206 blockers: 20 μ M Bicuculline, $n = 2$; 20 μ M Gabazine, $n = 1$. **I**, Representative multi-unit recordings

1207 of SST+ interneuron activity during step photo-excitation, showing average spike waveform,
 1208 autocorrelation, phase and step histogram. **J-K** Mean spike time histograms during step
 1209 illumination (**J**) and sinusoidal theta stimulation (8 Hz; **K**), calculated from the fraction of total
 1210 spike counts in each bin for each clustered neuron. **L**, Spike phase histograms relative to ongoing
 1211 gamma-frequency oscillations, calculated from the fraction of total spike counts. **M**, Sustained
 1212 activation index (top), modulation index (middle) and vector length (bottom).

1213

1214 **Figure 9: Computational model of the network effects of optogenetic modulation of interneuron**
 1215 **activity. A**, Schematic of connectivity between excitatory cells (E) and PV+ and SST+ interneurons.
 1216 E and PV+ cells were modelled using Wilson-Cowan equations and SST+ using equations derived
 1217 from quadratic integrate-and-fire neurons, which can show intrinsic oscillations (~). **B**, Activity
 1218 patterns observed in the 3 populations of cells when external drive to E cells is 10, and following
 1219 inhibition (Arch; top) or excitation (Chr2; bottom) of either PV+ (left) or SST+ (right) populations.
 1220 *Inset left*: expansion of traces highlighted by the dashed box during the baseline period, showing
 1221 temporal order of peak activity. *Inset right*: expansion of E cell activity during the period shown by
 1222 the dashed lines, showing small and fast oscillations. **C**, Corresponding changes in peak power
 1223 (top) and oscillation frequency (bottom), following manipulation of the external drive to PV+ (left)
 1224 or SST+ (right) populations. **D**, Plot of spike rate of E cells versus PV+ cells for the manipulations of
 1225 PV+ cells (left) and plot of spike rate of E cells versus SST+ cells for manipulation of SST+ cells
 1226 (right). The colour of each marker represents the frequency of the network oscillation and the size
 1227 of the marker reflects peak power. Black lines join the points showing spike rates during the
 1228 baseline conditions. **E**, Delays between the peak in E cell activity and the peak in activity for PV+
 1229 and SST+ cells across different manipulations. The size of the marker reflects the corresponding
 1230 spike rate. **F**, Light-induced decreases in both excitatory drive and presynaptic release, aimed at

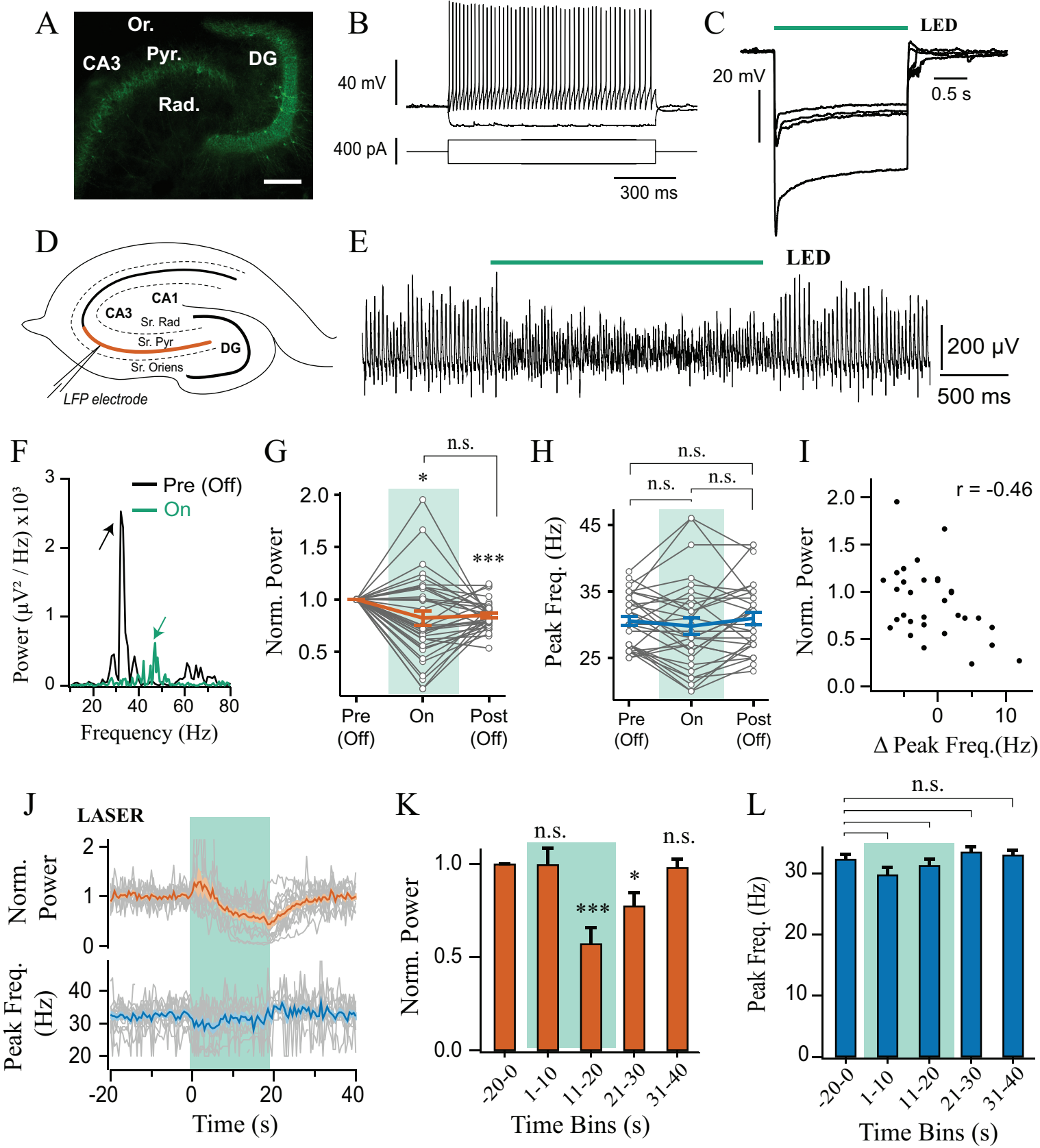
1231 mimicking laser stimulation of Arch, can lead to the collapse of the oscillations when applied to
 1232 either the PV+ (left) or SST+ (right) populations.

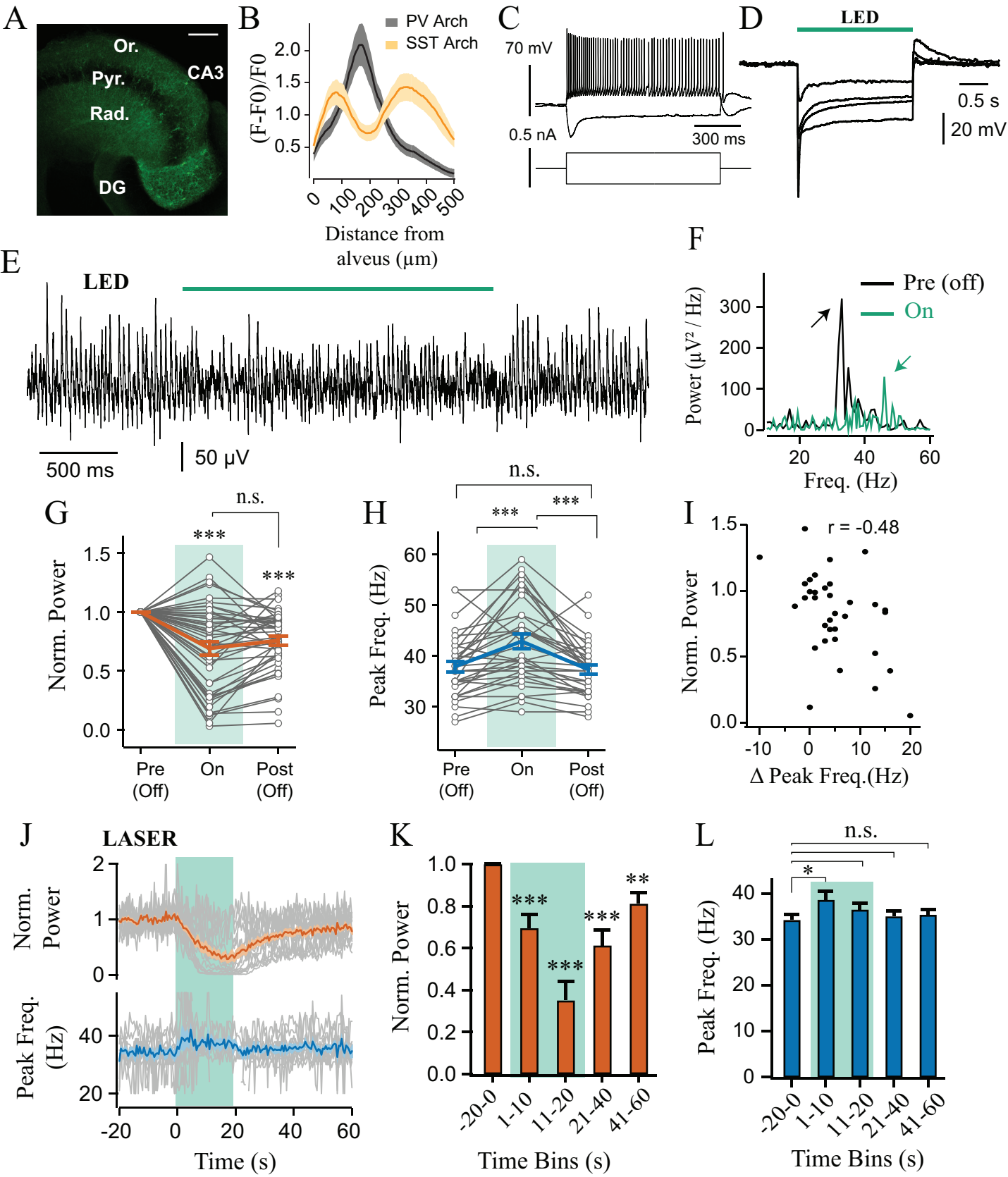
1233

1234 **Tables**

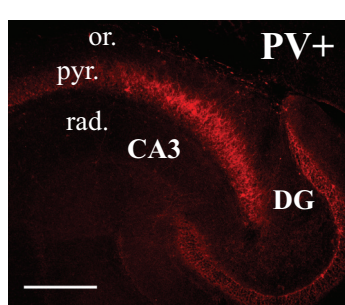
	Synaptic weights				Synaptic time constants (ms)		
<div>post</div> <div>pre</div>	<i>E</i>	<i>PV</i>	<i>SST</i>		<i>E</i>	<i>PV</i>	<i>SST</i>
<i>E</i>	10	30	10		10	3	5
<i>PV</i>	-15	-10			7	7	
<i>SST</i>	-15		-10		10		10

1235
 1236 Table 1. Synaptic parameters. *E* – excitatory neurons; *PV* - PV+ inhibitory neurons;
 1237 *SST* – SST+ inhibitory neurons.

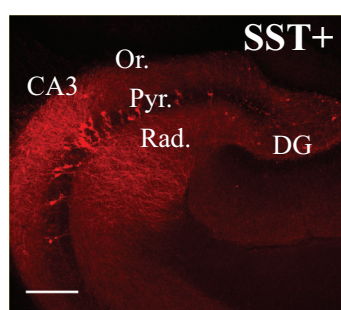




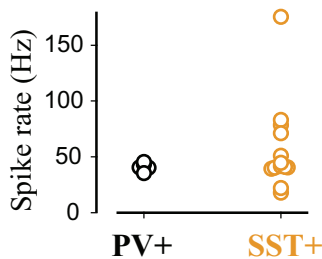
A



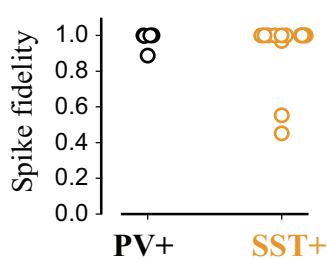
B



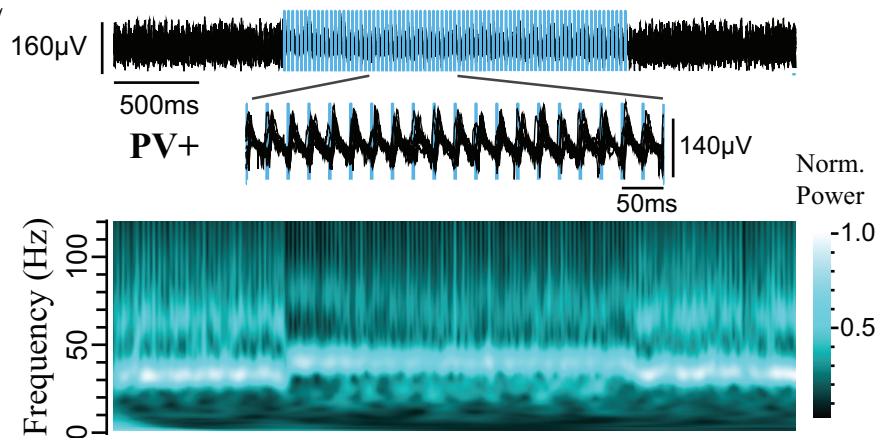
C



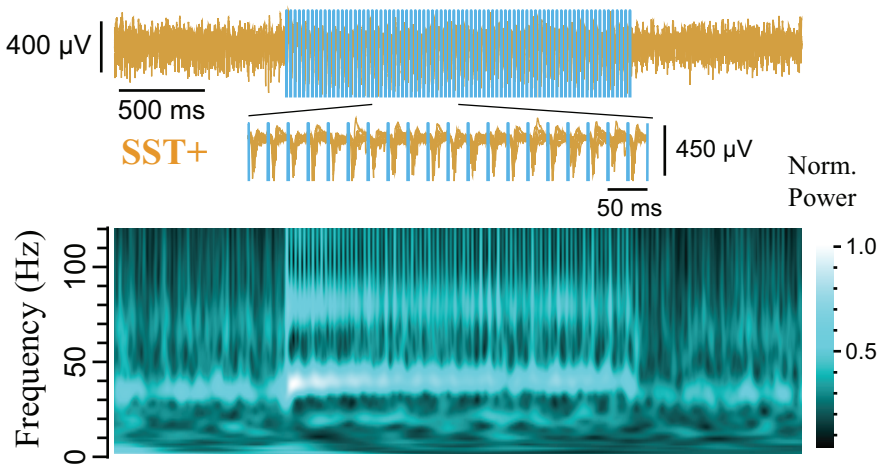
D



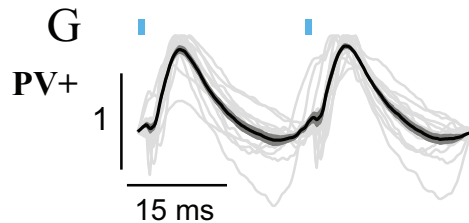
E



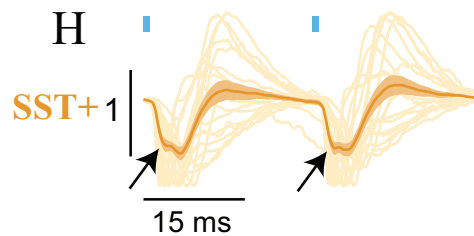
F



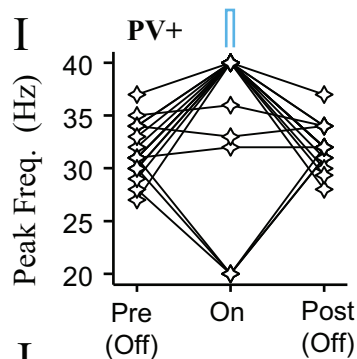
G



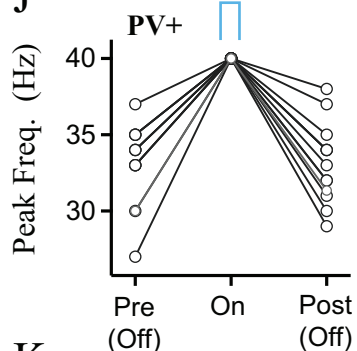
H



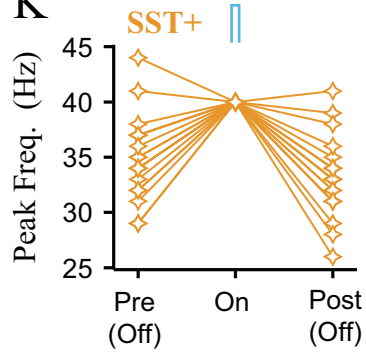
I

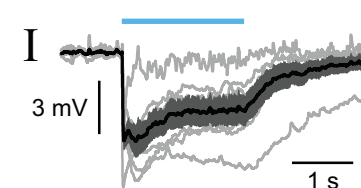
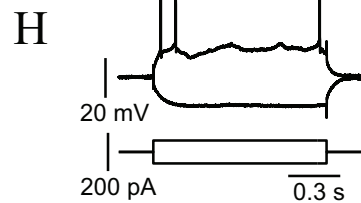
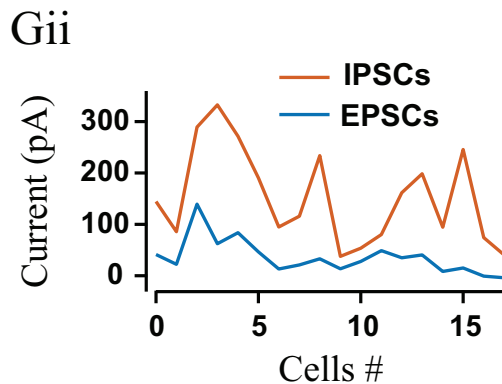
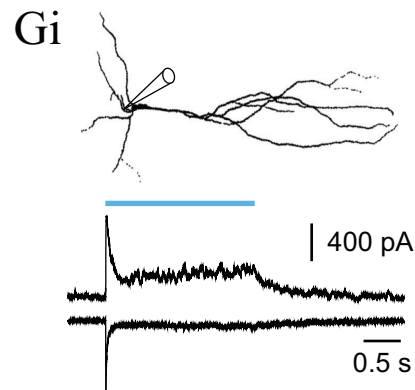
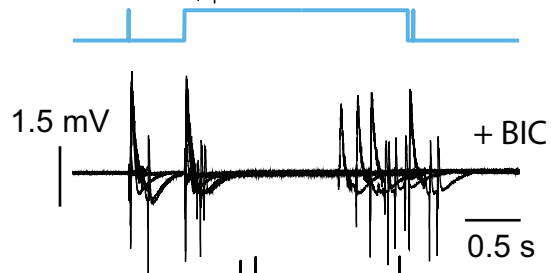
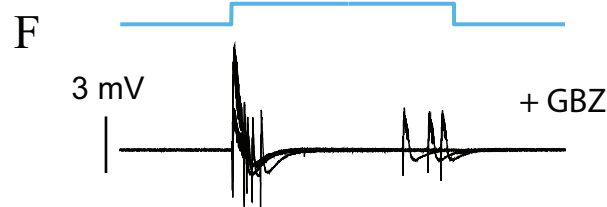
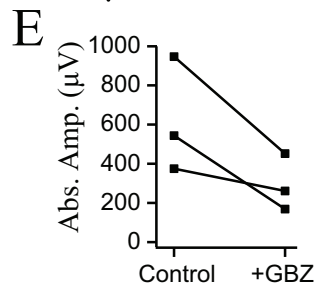
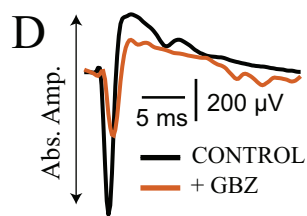
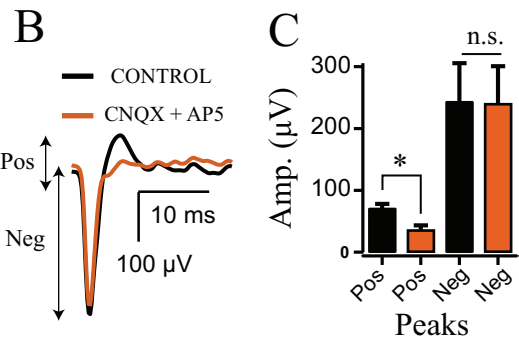
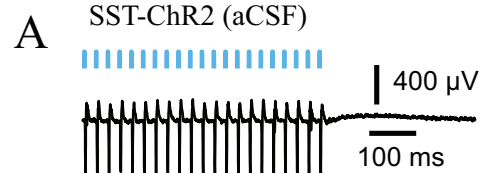


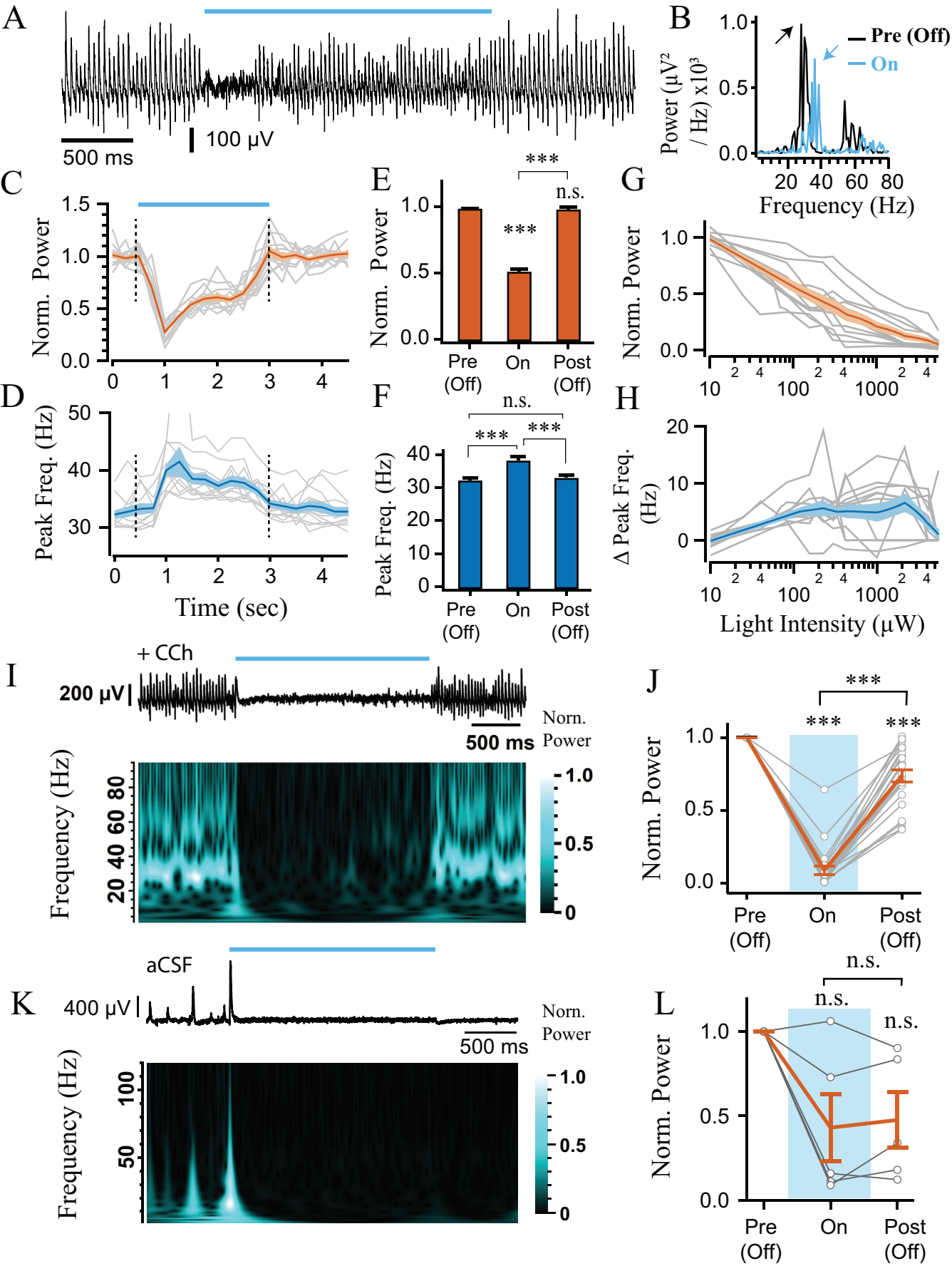
J

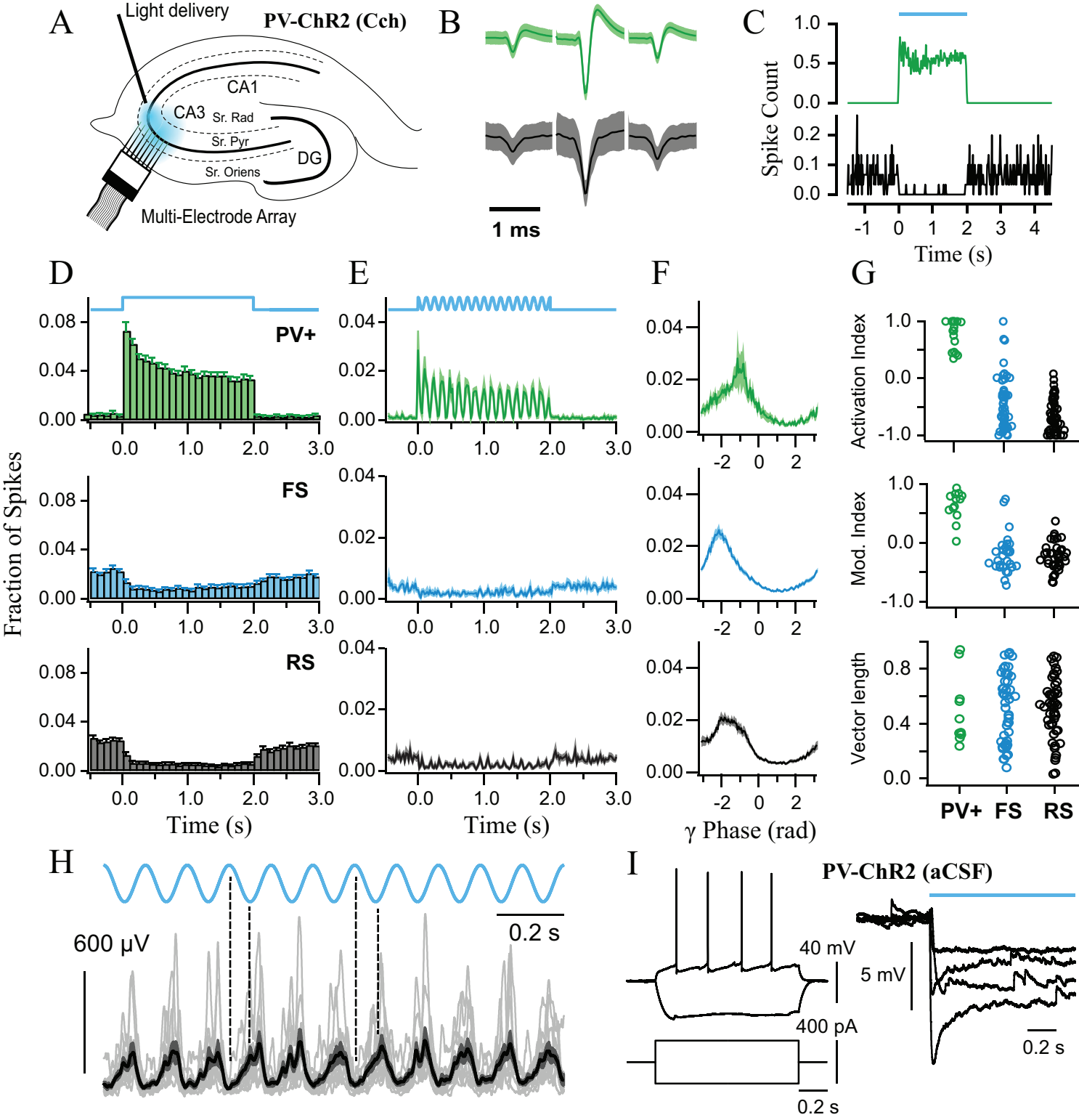


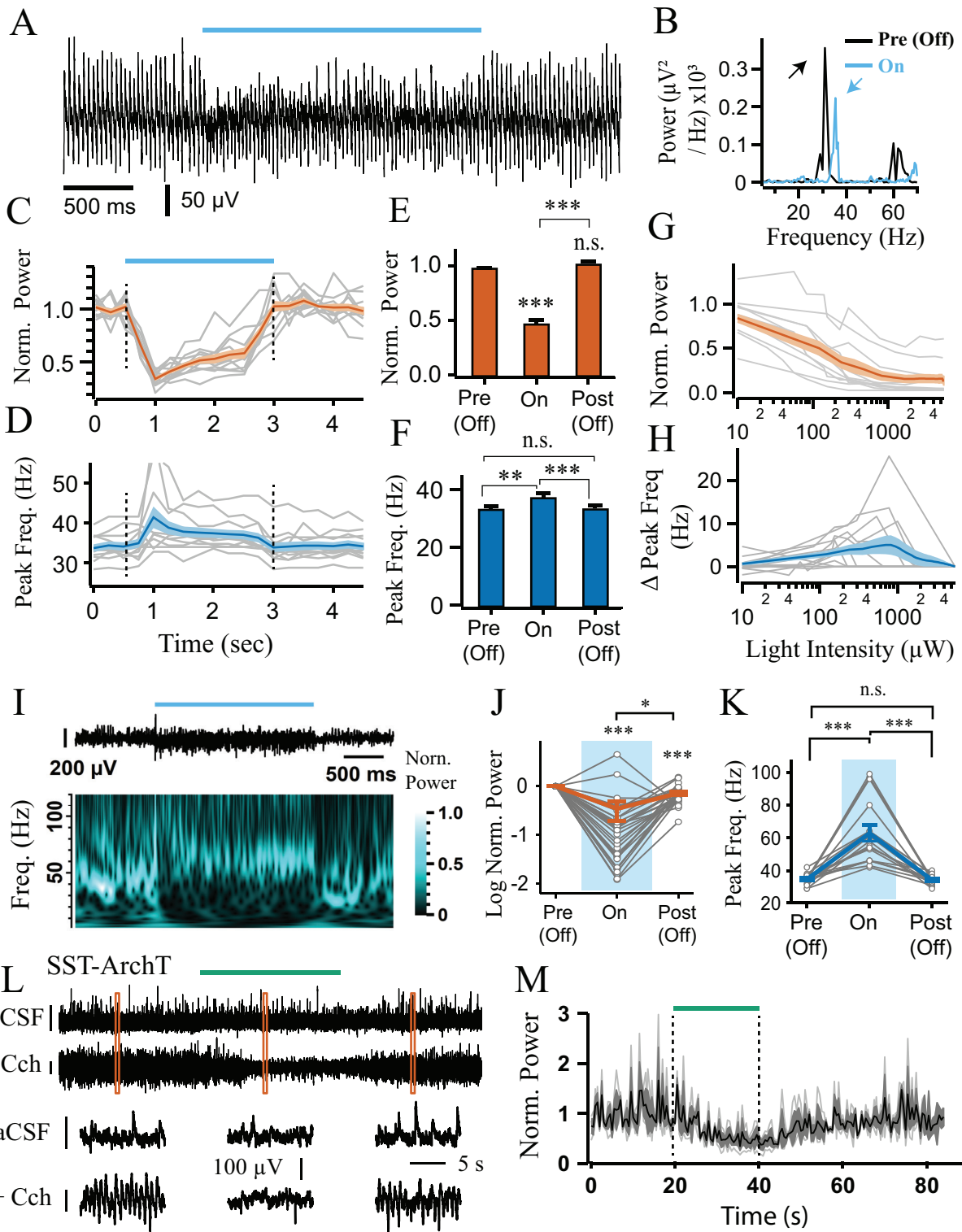
K

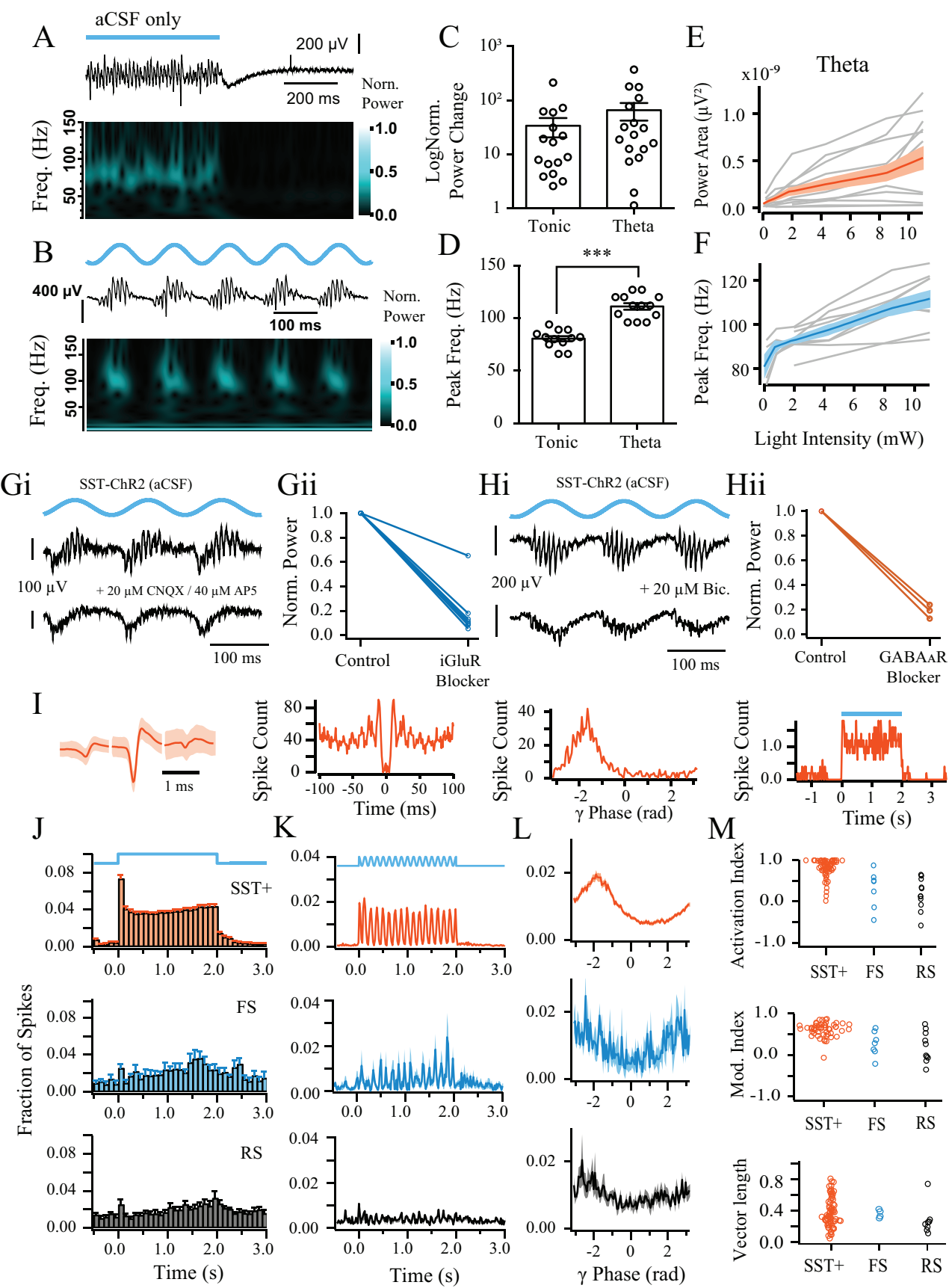


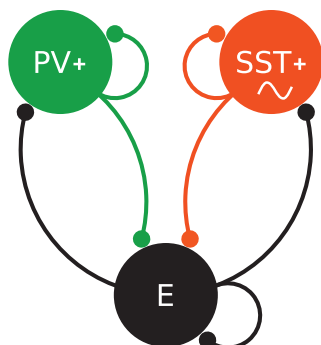
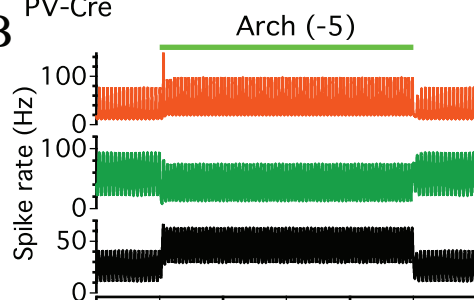




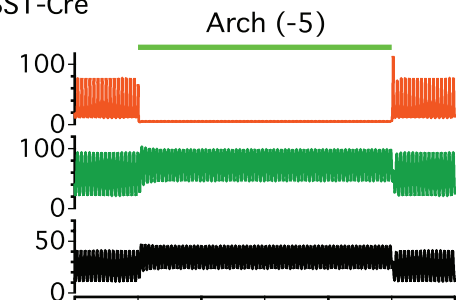
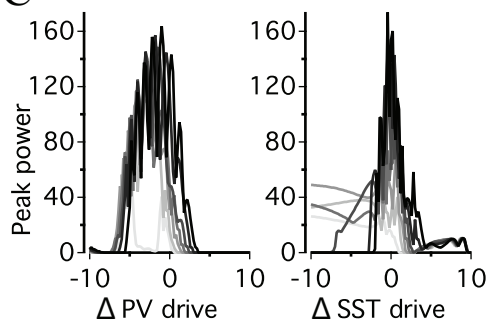
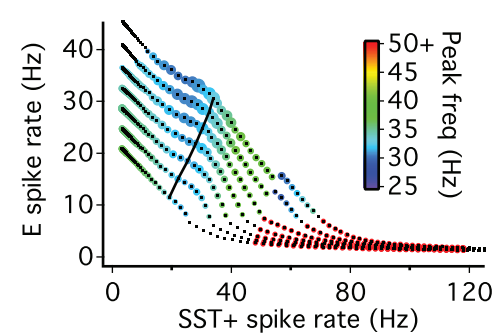
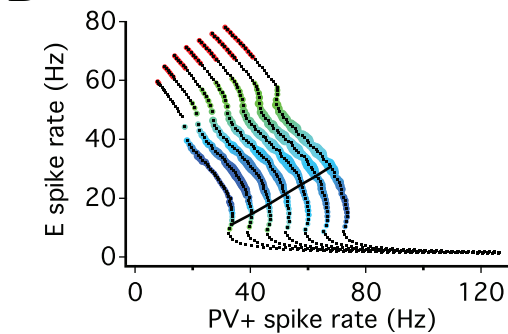
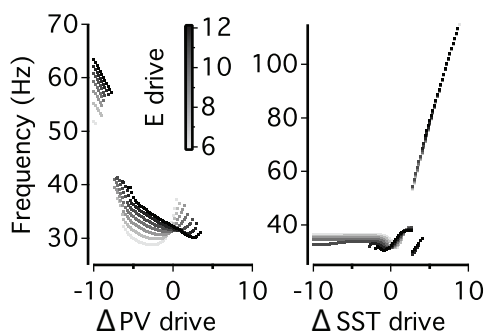
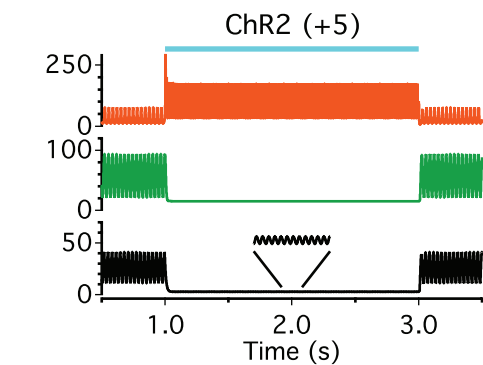
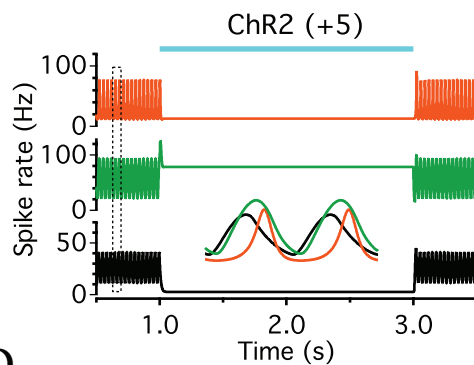
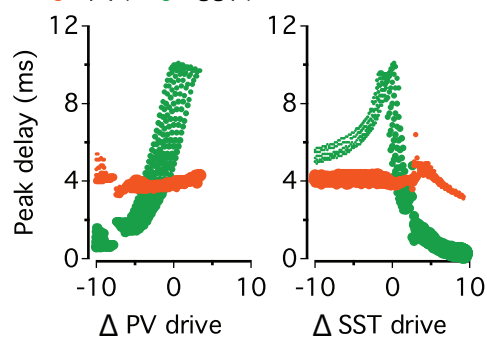






A**B**

SST-Cre

**C****D****E** ● PV+ ● SST+**F**